arXiv:1304.3320v3 [astro-ph.HE] 8 May 2013

SUPER LUMINOUS IC SUPERNOVAE: CATCHING A MAGNETAR BY THE TAIL

C. Inserra[1], S. J. Smartt[1], A. Jerkstrand[1], S. Valenti[2,3], M. Fraser[1], D. Wright[1], K. Smith[1], T.-W. Chen[1], R. Kotak[1], A. Pastorello[4], M. Nicholl[1], F. Bresolin[5], R. P. Kudritzki[5], S. Benetti[4], M. T. Botticella[6], W. S. Burgett[5], K. C. Chambers[5], M. Ergon[7], H. Flewelling[5], J. P. U. Fynbo[8], S. Geier[8,9], K. W. Hodapp[5], D. A. Howell[2,3], M. Huber[5], N. Kaiser[5], G. Leloudas[10,8], L. Magill[1], E. A. Magnier[5], M. G. McCrumm[1], N. Metcalfe[11], P. A. Price[5], A. Rest[12], J. Sollerman[7], W. Sweeney[5], F. Taddia[7], S. Taubenberger[13], J. L. Tonry[5], R. J. Wainscoat[5], C. Waters[5], and D. Young[1].

Draft version May 9, 2013

ABSTRACT

We report extensive observational data for five of the lowest redshift Super-Luminous Type Ic Supernovae (SL-SNe Ic) discovered to date, namely PTF10hgi, SN2011ke, PTF11rks, SN2011kf and SN2012il. Photometric imaging of the transients at +50 to +230 days after peak combined with host galaxy subtraction reveals a luminous tail phase for four of these SL-SNe. A high resolution, optical and near infrared spectrum from *xshooter* provides detection of a broad He I $\lambda10830$ emission line in the spectrum (+50d) of SN2012il, revealing that at least some SL-SNe Ic are not completely helium free. At first sight, the tail luminosity decline rates that we measure are consistent with the radioactive decay of ^{56}Co, and would require 1-4 $M_\odot$ of ^{56}Ni to produce the luminosity. These ^{56}Ni masses cannot be made consistent with the short diffusion times at peak, and indeed are insufficient to power the peak luminosity. We instead favour energy deposition by newborn magnetars as the power source for these objects. A semi-analytical diffusion model with energy input from the spin-down of a magnetar reproduces the extensive lightcurve data well. The model predictions of ejecta velocities and temperatures which are required are in reasonable agreement with those determined from our observations. We derive magnetar energies of $0.4 \lesssim E(10^{51}\text{erg}) \lesssim 6.9$ and ejecta masses of $2.3 \lesssim M_{\rm ej}(M_\odot) \lesssim 8.6$. The sample of five SL-SNe Ic presented here, combined with SN 2010gx - the best sampled SL-SNe Ic so far - point toward an explosion driven by a magnetar as a viable explanation for all SL-SNe Ic.

Subject headings: supernovae: general - supernovae: individual (PTF10hgi, SN 2011ke, PTF11rks, SN 2011kf, SN 2012il) - stars: magnetars

1. INTRODUCTION

The discovery of unusually luminous optical transients by modern supernova (SN) surveys has dramatically expanded the observational and physical parameter space of known SN types. The Texas Supernova Search was a pioneer in this area, with one of the first searches of the local Universe without a galaxy bias (Quimby et al. 2005). This has been followed by deeper, wider surveys from the Palomar Transient Factory (PTF, Rau et al. 2009), the Panoramic Survey Telescope & Rapid Response System (Pan-STARRS, Kaiser et al. 2010), the Catalina Real-time Transient Survey (CRTS, Drake et al. 2009), and the La Silla QUEST survey (Hadjiyska et al. 2012), all of which have found unusually luminous transients which tend to be hosted in intrinsically faint galaxies. These Super-Luminous SNe (SL-SNe) show absolute magnitudes at maximum light of $M_{\rm AB} < -21$ mag and total radiated energies of order 10^{51} erg. They are factors of 5 to 100 brighter than Type Ia SNe or normal core-collapse events. Gal-Yam (2012) proposed that three distinct physical groups of SL-SNe have emerged. The first group which was recognised was the luminous Type IIn SNe epitomised by SN 2006gy (Smith et al. 2007; Smith & McCray 2007; Ofek et al. 2007; Agnoletto et al. 2009) which show signs of strong circumstellar interaction. The second group includes Type Ic SNe that have broad, bright lightcurves and the decay rates imply that they could be due to pair-instability explosions powered by large ejecta masses of ^{56}Ni (3–5 $M_\odot$). To date only one object of this type (SN 2007bi) has been published and studied in detail (Gal-Yam et al. 2009; Young et al. 2010). The third group was labelled by Gal-Yam (2012) as Super-Luminous Type I Supernovae, or "SLSN-I"

[1] Astrophysics Research Centre, School of Mathematics and Physics, Queens University Belfast, Belfast BT7 1NN, UK; c.inserra@qub.ac.uk
[2] Las Cumbres Observatory Global Telescope Network, 6740 Cortona Dr., Suite 102 Goleta, Ca 93117
[3] Department of Physics, University of California, Santa Barbara, Broida Hall, Mail Code 9530, Santa Barbara, CA 93106-9530, USA
[4] INAF, Osservatorio Astronomico di Padova, vicolo dell'Osservatorio 5, 35122, Padova, Italy
[5] University of Hawaii, Institute of Astronomy, 2680 Woodlawn Drive, Honolulu, Hawaii 96822 USA
[6] INAF - Osservatorio astronomico di Capodimonte, Salita Moiariello 16, I- 80131 Napoli, Italy
[7] The Oskar Klein Centre, Department of Astronomy, AlbaNova, Stockholm University, 10691 Stockholm, Sweden
[8] Dark Cosmology Centre, Niels Bohr Institute, University of Copenhagen, 2100 Copenhagen, Denmark
[9] Nordic Optical Telescope, Apartado 474, E-38700 Santa Cruz de La Palma, Spain
[10] The Oskar Klein Centre, Department of Physics, Stockholm University, 10691 Stockholm, Sweden
[11] Department of Physics, Durham University, South Road, Durham DH1 3LE
[12] Space Telescope Science Institute, 3700 San Martin Drive, Baltimore, MD 21218, USA
[13] Max-Planck-Institut für Astrophysik, Karl-Schwarzschild-Str. 1, 85741 Garching, Germany

and the two earliest examples are SCP-06F6 and SN 2005ap (Barbary et al. 2009; Quimby et al. 2007) which are characterized at early times by a blue continuum and a distinctive "W"-shaped spectral feature at ∼4200 Å. In this paper we will call this type Super-Luminous Supernovae of Type Ic (or SL-SNe Ic), simply because they are Type Ic in the established supernova nomenclature and are extremely luminous.

The existence of this class of SL-SNe Ic was firmly established when secure redshifts were determined with the identification of narrow Mg II $\lambda\lambda2796,2803$ absorption from the host galaxies in the optical spectra of $z > 0.2$ transients by Quimby et al. (2011a). The spectra of four PTF transients, SCP-06F6 and SN 2005ap were then all linked together with these redshifts establishing a common type (Quimby et al. 2011a). Subsequently, the identification of host galaxy emission lines such as [O II] $\lambda3727$, [O III] $\lambda\lambda1959,5007$, Hα and Hβ has confirmed the redshift derived from the Mg II absorption in many SL-SNe Ic, such as in the case of SN 2010gx (Quimby et al. 2010; Mahabal & Drake 2010; Pastorello et al. 2010). These distances imply an incredible luminosity with $u-$ and $g-$band absolute magnitudes reaching about -22. This luminosity allowed these SNe to be easily identified in the Pan-STARRS Medium Deep fields at $z \sim 1$ (Chomiuk et al. 2011) and beyond (Berger et al. 2012).

The typical spectroscopic signature of the class of SL-SNe Ic is a blue continuum with broad absorption lines of intermediate mass elements such as C, O, Si, Mg with velocities $10000 < v < 20000$ km s^{-1}. No clear evidence of H or He has been found so far in the spectra of SL-SNe Ic, whereas Fe, Mg and Si lines are typically prominent after maximum. The study of the well sampled SN 2010gx (Pastorello et al. 2010) showed an unexpected transformation from a SL-SN Ic spectrum to that of a normal Type Ic SN. A similar transformation was also observed in the late-time spectrum of PTF09cnd (Quimby et al. 2011a), which evolved to become consistent with a slowly evolving Type Ic SN.

The SL-SNe Ic discovered to date appear to be associated with faint and metal poor galaxies at redshifts ranging between $0.23 - 1.19$ (typically $M_g > -17$ mag, Quimby et al. 2011a; Neill et al. 2011; Chomiuk et al. 2011; Chen et al. 2013), although the highest redshift SL-SNe Ic (PS1-12bam, $z = 1.566$) is in a galaxy which is more luminous and more massive than the lower redshift counterparts (Berger et al. 2012). An estimate of the metallicity of the faint host galaxy of SN 2010gx, from the detection of the auroral [O III] $\lambda4363$ line indicates a very low metallicity of 0.05 Z$_\odot$ (Chen et al. 2013). Research on SL-SNe Ic is progressing rapidly, with thirteen of these intriguing transients now identified since the discovery of SCP-06F6. To power the enormous peak luminosity of SL-SNe Ic with radioactive decay would require several solar masses of ^{56}Ni. However, this is inconsistent with the width of the lightcurves as shown by Chomiuk et al. (2011). The lightcurves cannot be reproduced with a physical model that has an ejecta mass significantly greater than the ^{56}Ni mass needed to power the peak. In the case of SN 2010gx, Chen et al. (2013) showed that the tail phase faded to levels which would imply an upper limit of around 0.4M$_\odot$ of ^{56}Ni.

Among the scenarios proposed to explain the remarkable peak luminosity are the spin down of a rapidly rotating young magnetar (Kasen & Bildsten 2010; Woosley 2010), that provides an additional reservoir of energy for the SN (Ostriker & Gunn 1971; Usov 1992; Wheeler et al. 2000; Thompson et al. 2004); the interaction of the SN ejecta with a massive (3-5 M$_\odot$) C/O-rich circumstellar medium (CSM, Blinnikov & Sorokina 2010) or with a dense wind (Chevalier & Irwin 2011; Ginzburg & Balberg 2012); or collisions between high velocity shells ejected by a pulsational pair instability, which would give rise to successive bright optical transients (Woosley et al. 2007). One of these SNe (SN 2006oz) was discovered 29 days before peak luminosity and showed a flat plateau in the rest-frame NUV before its rise to maximum, indicating that finding these objects early could give constraints on the explosion channel (Leloudas et al. 2012). In most cases to date however, the lightcurves and energy released at >100d is unexplored territory. Chen et al. (2013) quantified host of SN2010gx, but difference imaging showed no detection of SN flux at 250-300 days to deep limits. Quimby et al. (2011a) detected flux at the position of PTF09cnd at +138d after peak in a B-band image, but it's not clear if this flux is from the host or the SN. In this paper we present the detailed follow-up of five SL-SNe Ic at $0.100 < z < 0.245$, namely PTF11rks, SN 2011ke, SN 2012il, PTF10hgi and SN 2011kf, and attempt to follow them for as long as possible to garner further evidence to probe the physical mechanism powering these intriguing events. A detailed analysis of their hosts will be part of a future paper (Chen et el. in prep).

The paper is organized as follows: in Sect. 2 we introduce the SNe, and report distances and reddening values. Photometric data, light and colour curves as well as the absolute light curves in the rest-frame are presented in Sect. 3. Sect. 4 is devoted to the analysis of bolometric and pseudo-bolometric light curves and the evaluation of possible ejected ^{56}Ni masses, while in Sect. 5 we describe and analyse the spectra. Finally, a discussion about the origin of these transients is presented in Sect. 6, followed by a short summary in Sect. 7.

2. DISCOVERY AND TARGET SAMPLE

2.1. *Pan-STARRS1 data : discovery and recovery of the transients*

The strong tendency for these SL-SNe to be hosted in faint galaxies appears not to be a bias, which suggests a straightforward way of finding them in large volume, wide-field searches. With the Pan-STARRS1 survey, we have been running the "Faint Galaxy Supernova Survey" (FGSS) which is aimed at finding transients in faint galaxies originally identified in the Sloan Digital Sky Survey catalogue (Valenti et al. 2010).

The Pan-STARRS1 optical system uses a 1.8m diameter aspheric primary mirror, a strongly aspheric 0.9m secondary and 3-lens corrector and has 8m focal length (Hodapp et al. 2004). The telescope illuminates a diameter of 3.3 degrees and the "GigaPixel Camera" (Tonry & Onaka 2009) comprises a total of 60 4800×4800 pixel detectors, with 10 μm pixels that subtend 0.258 arcsec (for more details see Magnier et al. 2013). The PS1 filter system is described in Tonry et al. (2012), and is similar to but not identical to the SDSS

TABLE 1
MAIN PROPERTIES OF THE SN SAMPLE.

	PTF10hgi	SN 2011ke	PTF11rks	SN 2011kf	SN 2012il
Alternative names	PSO J249.4461+06.20815	PS1-11xk, PTF11idj, CSS110406: 135058+261642		CSS111230: 143658+163057	PS1-12fo CSS120121: 094613+195028
α (J2000.0)	$16^h37^m47^s.08$	$13^h50^m57^s.78$	$01^h39^m45^s.49$	$14^h36^m57^s.64$	$09^h46^m12^s.91$
δ (J2000.0)	$06°12'29''.35$	$26°16'42''.40$	$29°55'26''.87$	$16°30'57''.17$	$19°50'28''.70$
z	0.100	0.143	0.190	0.245	0.175
Peak g (mag)	-20.42	-21.42	-20.76	-21.73	-21.56
E(B-V) (mag)	0.09	0.01	0.04	0.02	0.02
L_{griz} peak (x 10^{43} erg s^{-1})	2.09	4.47	3.24	6.45	$\gtrsim 4.47$
Light curve peak (MJD)	55326.4 ± 4.0	55686.5 ± 2.0	55932.7 ± 2.0	55925.5 ± 3.0	55941.4 ± 3.0
Host r (mag)	-16.50	-18.42	-19.02	-16.52	-18.18

$griz$ (York et al. 2000) filter system. However it is close enough that catalogued cross-matching between the surveys can identify high amplitude transients. In this paper we will convert all the PS1 filter magnitudes $g_{P1}r_{P1}i_{P1}z_{P1}y_{P1}$ to the SDSS AB magnitude system as the bulk of the follow-up data were taken in SDSS-like filters (see Section 3 for more details).

The PS1 telescope is operated by the PS1 Science Consortium (PS1SC) to undertake several surveys, with the two major ones being the "Medium Deep Field" survey (e.g Botticella et al. 2010; Tonry et al. 2012; Gezari et al. 2012; Berger et al. 2012) which was optimised for transients (allocated around 25% of the total telescope time) and the wide-area 3π Survey, allocated around 56% of the available observing time. As described in Magnier et al. (2013), the goal of the 3π Survey is to observe the portion of the sky North of -30 deg declination, with a total of 20 exposures per year across all five filters for each field center. The 3π survey plan is to observe each field center 4 times in each of $g_{P1}r_{P1}i_{P1}z_{P1}y_{P1}$ during a 12 month period, although this can be interrupted by bad weather. As described by Magnier et al. (2013), the 4 epochs in a calendar year are typically split into two pairs called Transient Time Interval (TTI) pairs which are single observations separated by 20-30 minutes to allow for the discovery of moving objects. The temporal distribution of the two sets of TTI pairs is not a well defined and straightforward schedule. The blue bands (g_{P1}, r_{P1}, i_{P1}) are scheduled close to opposition to enhance asteroid discovery with g_{P1} and r_{P1} being constrained in dark time as far as possible. The z_{P1} and y_{P1} filters are scheduled far opposition to optimise for parallax measurements of faint red objects. Although a large area of sky is observed each night (typically 6000 square degrees), the moving object and parallax constraints mean the 3π survey is not optimised for finding young, extragalactic transients in a way that the Palomar Transient Factory and La Silla-QUEST projects are. The exposure times at each epoch (i.e. in *each* of the TTI exposures) are 43s, 40s, 45s, 30s and 30s in $g_{P1}r_{P1}i_{P1}z_{P1}y_{P1}$. These reach typical 5σ depths of roughly 22.0, 21.6, 21.7, 21.4. 19.3 as estimated from point sources with uncertainties of 0.2^m. (in the PS1 AB magnitude system described by Tonry et al. 2012).

The PS1 images are processed by the Pan-STARRS1 Image Processing Pipeline (IPP), which performs automatic bias subtraction, flat fielding, astrometry (Magnier et al. 2008) and photometry (Magnier 2007). These photometrically and astrometrically calibrated

catalogues produced in MHPCC are made available to the PS1SC on a nightly basis and are immediately ingested into a MySQL database at Queen's University Belfast. We apply a tested rejection algorithm and cross match the PS1 objects with SDSS objects in the DR7 catalogue[14] (Abazajian et al. 2009). We apply the following selection filters to the PS1 data (all criteria must be simultaneously fulfilled)

- PS1 source must have $15 < g_{P1} < 20$ or $15 < r_{P1} < 20$ or $15 < i_{P1} < 20$ or $15 < z_{P1} < 20$

- SDSS counterpart must have $18 < r_{SDSS} < 23$

- Distance between PS1 source and SDSS source < 3 arcsec

- PS1 mag must be 1.5 mag brighter than SDSS (in the corresponding filter)

- The PS1 object must be present in both TTI pairs and the astrometric recurrences $< 0.3''$. Objects with multiple detections must have RMS scatter $< 0.1''$

- The PS1 object must not be in the galactic plane ($|b| > 5°$).

All objects are then displayed through a Django-based interface to a set of interactive webpages, and human eyeballing and checking takes place. We use the star-galaxy separation in SDSS to guide us in what may be variable stars (i.e. stellar sources in SDSS which increase their luminosity) or extragalactic transients (i.e. QSOs, AGNs and SNe). While the cadence of the PS1 observations is not ideal for detections of young SNe we have found many SNe in intrinsically faint galaxies. As of January 2013, spectroscopically confirmed objects include 34 QSOs or AGNs and 41 SNe. Several of these have been confirmed as SL-SNe. Pastorello et al. (2010) presented the data of SN 2010gx recovered in 3π images, and in many cases the same object is detected by the Catalina Real-Time Transient Survey (CSS/MSS) and PTF. As we are not doing difference imaging and only comparing to objects in the SDSS footprint, there are some cases where objects are reported by PTF or CRTS and interesting pre-discovery epochs are available in PS1. As 3π difference imaging is not being carried out routinely, we often use the PTF and CRTS announcements to inform

---

[14] http://www.sdss.org/dr7/

a retrospective search. In this paper, we present five SL-SNe Ic which were either detected through the PS1 Faint Galaxy Supernova Survey, or were announced in the public domain. A sixth object (PTF12dam≡PS1-12arh) is discussed in a companion paper (Nicholl et al. in prep.). In all five cases follow-up imaging and spectroscopy was carried out as discussed below.

For all the SNe listed here (and throughout this paper) we adopt a standard cosmology with $H_0 = 72$ km s^{-1}, $\Omega_{\mathrm{M}} = 0.27$ and $\Omega_\lambda = 0.73$. There is no detection of Na I interstellar medium (ISM) features from the host galaxies, nor do we have any evidence of significant extinction in the hosts from the SNe themselves. This suggests that the absorption in host is low and we assume that extinction from the host galaxies is negligible. Although we do detect Mg II ISM lines from the hosts in some cases, there is no clear correlation with these line strengths and line of sight extinction. In all cases only the Milky Way foreground extinction was adopted.

2.2. *PTF10hgi*

PTF10hgi was first discovered by PTF on 2010 May 15.5 and announced on 2010 July 15 (Quimby et al. 2010). The spectra taken by PTF on May 21.0 UT and June 11.0 UT were reported as a blue continuum with faint features typical of SL-SNe Ic. Another spectrum obtained by PTF on July 7.0 UT was similar to PTF09cnd at 3 weeks past peak brightness. Initiated by Quimby et al. (2010), UV observations were obtained with Swift+UVOT in July 2010, and we analyse those independently later in Sect.3. PTF10hgi lies outside the SDSS DR9[15] area (Ahn et al. 2012), hence was not discovered by our PS1 FGSS software. However after the announcement (Quimby et al. 2010), we recovered it in PS1 images taken (in band r_{P1}) on 2010 May 18 and on 4 other epochs around peak magnitude (in bands $g_{\mathrm{P1}}r_{\mathrm{P1}}i_{\mathrm{P1}}$), listed in Table 5.

We detect a faint host galaxy in deep $griz$-band images taken with the William Herschel Telescope on 2012 May 26 and the Telescopio Nazionale Galileo on 2012 May 28. At a magnitude $r = 22.01 \pm 0.07$, this is too faint to affect the measurements of the SN flux up to +90 days. There are no host galaxy emission lines detected in our spectra, hence the redshift is determined through cross-correlation of the spectra of PTF10hgi with other SNe at confirmed redshift indicating a redshift of $z = 0.100 \pm 0.014$, corresponding to a luminosity distance of $d_{\mathrm{L}} \sim 448$ Mpc. The Galactic reddening toward the SN line of sight is $E(B - V) = 0.09$ mag (Schlegel et al. 1998).

2.3. *SN 2011ke*

SN 2011ke was discovered in the CRTS (CSS110406:135058+261642) and PTF surveys (PTF11dij) with the earliest detections on 2011 April 06 and 2011 March 30 respectively (Drake et al. 2011; Quimby et al. 2011c). We also independently detected this transient in the PS1 FGSS (PS1-11xk) on images taken on 2011 April 15 (Smartt et al. 2011). However earlier PS1 data show that we can determine the epoch of explosion to around one day, at least as

far as the sensitivity of the images allow. On MJD 55649.55 (2011 March 29.55 UT) a PS1 image ($r_{\mathrm{P1}} = 40$s) shows no detection of the transient to $r \simeq 21.17$ mag. Quimby et al. (2011c) report the PTF detection on 2011 March 30 (MJD=55650) the night after the PS1 non-detection at $g \simeq 21$. PS1 detections then occurred 1 and 3 days after this on 55651.6 and 55653.6 (in i_{P1} and r_{P1}) respectively. The photometry is given in Table 6. This is the best constraint on the explosion epoch of an SL-SNe to date, allowing the rise time and light curve shape to be confidently measured. The object brightened rapidly, by ~ 3 mag in $g-$band in the first 15 days and 1.7 mag in the subsequent 20 days. It was classified as an SL-SNe Ic by both Drake et al. (2011) and Quimby et al. (2011c); their spectra obtained on May 8.0 and 11.0 UT, respectively, showed a blue continuum with faint features, similar to PTF09cnd about 1 week past maximum light (Quimby et al. 2011c).

We found a nearby source in the SDSS DR9 catalog ($g = 21.10 \pm 0.08$, $r = 20.71 \pm 0.08$), which is the host galaxy as confirmed by deep $griz$ images taken with the William Herschel Telescope on the 26th of May 2012 at a magnitude $g = 21.18 \pm 0.05$, $r = 20.72 \pm 0.04$. The host emission lines set the SN at $z = 0.143$, equivalent to a luminosity distance of $d_{\mathrm{L}} = 660$ Mpc. The Galactic reddening toward the position of the SN is $E(B - V) = 0.01$ mag (Schlegel et al. 1998).

2.4. *PTF11rks*

PTF11rks was first detected by PTF on 2011 December 21.0 UT (Quimby et al. 2011b). Spectra acquired on December 27.0 UT and 31.0 UT showed a blue continuum with broad features similar to PTF09cnd at maximum light, confirming it as a SL-SN Ic. A non-detection in the r-band on Dec. 11 UT prior to discovery is also reported, setting a limit of >20.6 mag at this epoch. Quimby et al. (2011b) detailed a brightening of 0.8 mag in r-band in the first 6 days after the discovery. Prompt observations with Swift revealed an ultraviolet (UV) source at the optical position of the SN, but no source was detected in X-rays at the same epochs. There are no useful early data from PS1 for this object.

The host galaxy is listed in the SDSS DR9 catalogue with $g = 21.59 \pm 0.11$ mag and $r = 20.88 \pm 0.10$ mag. Confirmation of these host magnitudes as achieved with our deep gr-band images taken with the William Herschel Telescope on the 22nd of September 2012 at a magnitude $g = 21.67 \pm 0.07$ and $r = 20.83 \pm 0.05$. The emission lines of the host and narrow absorptions consistent with Mg II $\lambda\lambda2796,2803$ doublet locate the transient at $z = 0.19$, corresponding to a luminosity distance of $d_{\mathrm{L}} = 904$ Mpc. The Galactic reddening toward the position of the SNe is $E(B - V) = 0.04$ mag (Schlegel et al. 1998).

2.5. *SN 2011kf*

SN 2011kf was first detected by CRTS (CSS111230:143658+163057) on 2011 December 30.5 UT (Drake et al. 2012). The spectra taken by Prieto et al. (2012) on 2012 January 2.5 UT and 17.5 UT reveal a blue continuum with absorption feature typical of a luminous Type Ic SN.

The closest galaxy is $\sim 23''$ S/W of the object position and is hence too far to be the host. There is no obvious

host coincident with the position of this SN in SDSS DR9. We detect a faint host galaxy in deep gri-band images taken with the William Herschel Telescope on 20 July 2012. At a magnitude $r = 23.94 \pm 0.20$, this is too faint to affect the measurements of the SN flux out to +120 days. The redshift of the object has been determined to be z=0.245 from narrow Hα and [O III], equivalent to a luminosity distance of $d_L = 1204$ Mpc. The foreground reddening is $E(B-V) = 0.02$ mag from Schlegel et al. (1998).

2.6. SN 2012il

SN 2012il was first detected in the PS1 FGSS on 2012 January 19.9 UT (Smartt et al. 2012) and also independently discovered by CRTS on the 21st of January 2012 (CSS120121:094613+195028 Drake et al. 2012). On January 29 UT we obtained a spectrum of the SN, which resembled SN 2010gx 4d after maximum light. The merged PS1 and CRTS data suggest a rise time of more than 2 weeks, different from that of SN 2010gx (Pastorello et al. 2010) but similar to PS1-11ky (Chomiuk et al. 2011). An initial analysis of observations from Swift revealed a marginal detection in the u, b, v and uvm2 filters, with no detection in the uvw1 and uvw2 filters, or in X-rays (Margutti et al. 2012). However our re-analysis of the Swift data reveals a detection above the 3σ level in the uvw1 and uvw2 filters (see Tab. 11). No radio continuum emission from the SN was detected by the EVLA (Chomiuk et al. 2012).

In our astrometrically calibrated images the SN coordinates are $\alpha = 09^h46^m12^s.91 \pm 0^s.05$, $\delta = +19°50'28''.70 \pm 0''.05$ (J2000). This is within 0.12" of the faint galaxy SDSS J094612.91+195028.6 ($g = 22.13 \pm 0.08$, $r = 21.46 \pm 0.07$). The emission lines of Hα, Hβ and [O III] from the host give a redshift of $z = 0.175$, corresponding to a luminosity distance of $d_L = 825$ Mpc. The Galactic reddening towards SN 2012il given by Schlegel et al. (1998) is $E(B-V) = 0.02$ mag, three times lower than the value reported by Margutti et al. (2012).

3. FOLLOW-UP IMAGING AND PHOTOMETRY

Optical and near infrared (NIR) photometric monitoring of the five SNe was carried out using the telescopes and instruments listed in Appendix A. The main sources of our photometric follow-up were the SDSS-like $griz$ filters in the cameras at the Liverpool Telescope (RATCam), William Herschel Telescope (ACAM), and the Faulkes North Telescope (MEROPE). Further data in BV and JHK filters were taken for some of the SNe with the EKAR 1.8m Telescope (AFOSC), the ESO NTT (EFOSC2) and the Nordic Optical Telescope (NOTCam). Swift+UVOT observations have been taken for four out of five SNe in the UV filters uvw2, uvm2 and uvw1 (and for three SNe in the Swift u filter) and we analysed these publicly available data independently. Aside from SN 2011ke, ground based SDSS-like u observations were sparse, and for two SNe of our sample nonexistent.

Observations were reduced using standard procedures in the IRAF[16] environment. The magnitudes of the

[16] Image Reduction and Analysis Facility, distributed by the National Optical Astronomy Observatories, which are operated by the Association of Universities for Research in Astronomy, Inc, under contract to the National Science Foundation.

SNe, obtained through a point spread function (PSF) fitting, were measured on the final images after overscan correction, bias subtraction, flat field correction and trimming. When necessary we applied a template subtraction technique on later epochs (through the HOTPANTS[17] package based on the algorithm presented in Alard 2000). The instruments used to obtain reference images were the William Herschel Telescope and the Telescopio Nazionale Galileo. The same images were used to measure the host magnitudes and listed in Appendix A (Tabs. 5, 6, 7, 9 & 10) and labelled as "Host". When we did not have template images, we used SDSS images as template to remove the flux of the host. The magnitudes of SDSS stars in the fields of the transients were used to calibrate the observed light curves (Fig. 2). All Sloan magnitudes - as well as the NTT U and R magnitudes - were converted to the SDSS AB magnitude system and colour corrections were applied. PS1 magnitudes were also converted to SDSS magnitudes following the prescription in Tonry et al. (2012). B and V magnitudes are reported in the Vega system. The PTF10hgi field was not covered by SDSS, so the average magnitudes of local sequence stars were determined on photometric nights, and subsequently used to calibrate the zero points for the non-photometric nights. Magnitudes of the local sequence stars are reported in Appendix B (Tab. 12) along with their rms (in parentheses).

For the Swift u band data, we determined magnitudes in the UVOT instrumental system (Poole et al. 2008) and subsequently converted to Sloan u by applying a shift of $\Delta u \approx 0.2$ mag. The shift has been computed for each SN from a comparison of the magnitudes of the reference stars in the SNe fields in the UVOT and Sloan photometric systems. The only exception is PTF10hgi, where due to the absence of ground-based u images, we applied the average shift of the other SNe. The UV magnitudes are reported in Appendix A (Tab. 11).

NIR observations are not shown in Fig. 2 as these were only obtained for PTF11rks. The JHK photometry was calibrated to the 2MASS system (Vega based), using the same local sequence stars as for the optical calibration. Thus the values reported are Vega magnitudes.

3.1. Light curves

3.1.1. PTF10hgi

Pre-peak observations are available only in the $r-$band, suggesting a rise time comparable to SN 2011ke. PTF10hgi shows a bell-like shaped light curve around peak. The post maximum lightcurve shows a constant decline in all the bands until 40d. After 40d, the decline rate of PTF10hgi changes to have a slope similar to the decays shown by the other SNe. The change in the $i-$band slope is not as evident, while the $z-$band light curve is also dissimilar to the other bands. The magnitudes beyond 90d are evaluated using the template subtraction with 646-648d epochs as template images.

3.1.2. SN 2011ke

SN 2011ke was detected during the rise phase, and we continued to observe the SN until it disappeared behind the Sun in late August 2011. The non-detection of the

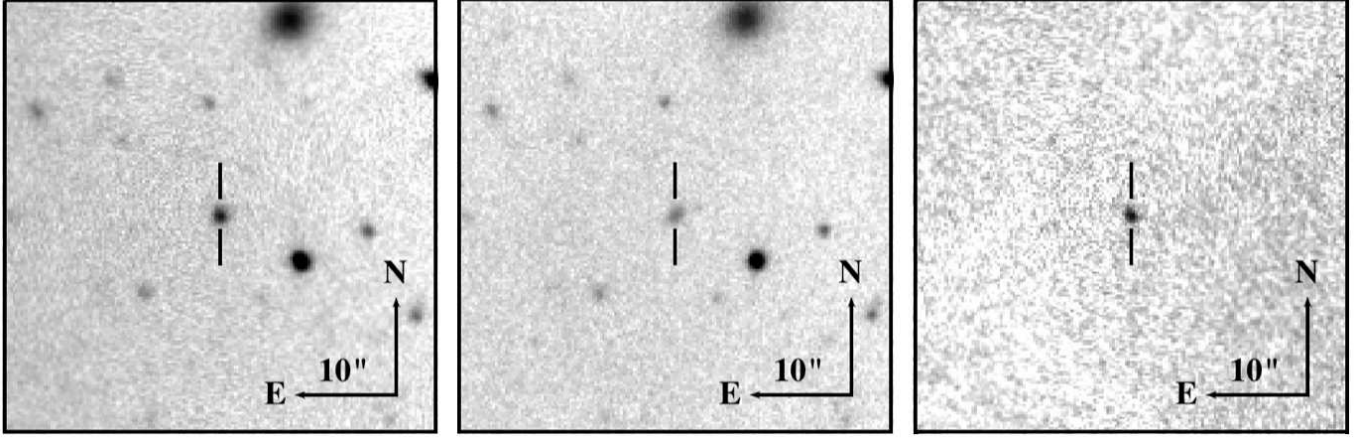[17] http://www.astro.washington.edu/users/becker/hotpants.html

FIG. 1.— From left to right: PTF10hgi+host galaxy on MJD 55615.2, host galaxy on MJD 56075.0 used as template image and the final subtracted image showing the SN.
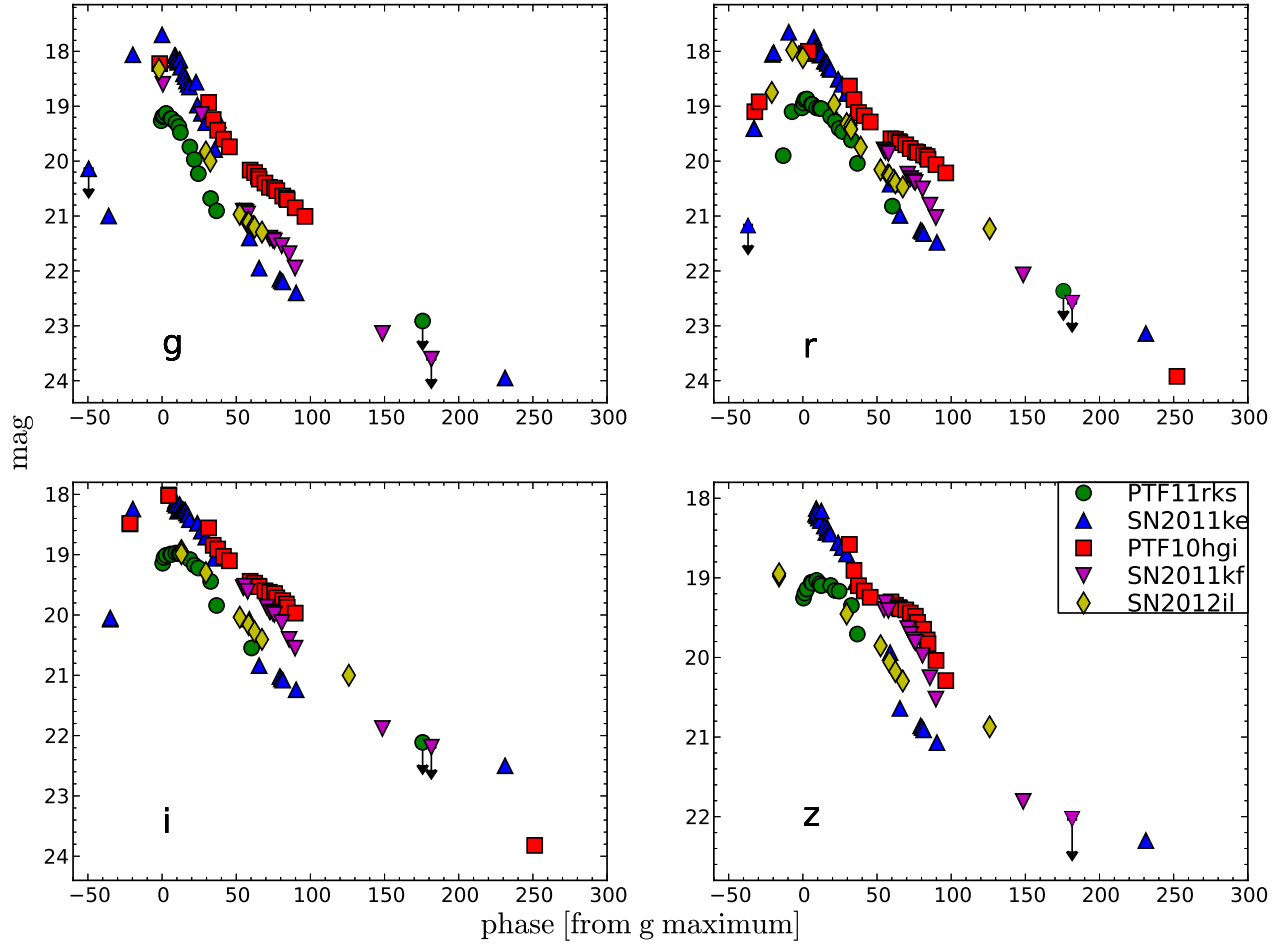

FIG. 2.— Observed g r i z light curves of PTF11rks (green circles), SN 2011ke (blue triangles), PTF10hgi (red squares) , SN 2011kf (purple upside-down triangles) and SN 2012il (gold diamonds). The phase is from the respective maximum in the g band. Detections from the ATels are shown here and reported in Appendix A, in Tabs. 5, 6, 7, 9 and 10.

transient the day before the discovery gives us the best constraint on the explosion epoch of any SL-SN to date, allowing the rise time and light curve shape to be confidently measured. The light curve is bell shaped around peak in the observed-frame $g-$band, and more similar to the light curve of SCP-06F6 (Barbary et al. 2009). The post maximum light decrease is slower at redder wavelengths, as in the previous object. It follows a constant slope until 50d, when the slope changes to a slower decline. SN 2011ke then continued to fade at the same rate until the last available photometric point at ~ 200d post maximum. The reference template (339d) was used to retrieve the magnitudes after 51d.

3.1.3. PTF11rks

The transient was discovered just before the $g-$band peak. The pre-discovery limit of December 11 (Quimby et al. 2011b) indicates a rise time on the order of 20 d, followed by a slower decline post-maximum. The $r-$band light curve shows an asymmetric peak as for SNe 2005ap and 2010gx (Quimby et al. 2007; Pastorello et al. 2010), in contrast to the rounded peaks of the light curves of PS1-10awh and PS1-10ky (Chomiuk et al. 2011). The SN fades by ~ 2.1 mag over the first 30d in rest frame g band, with a slower decline in the redder bands. The decrease is faster than that of the other SL-SNe Ic, although a more rapid decline at redder wavelengths is common in SNe (see Fig. 1 in Pastorello et al. 2010). After 50 days the SN faded below our detection limit, even in deep imaging. A small, but non-negligible, flux contribution from the host has been found after 28d and was removed using template subtraction with the reference images at 218d. While for the i and z bands we used the SDSS images as template.

3.1.4. SN 2011kf

The light curve of SN 2011kf is the least well sampled as our monitoring started some 20 days after the ATel discovery announcement. We assume that the reported point of Drake et al. (2012) is at peak which is supported by the spectral and colour evolution of the SL-SN during its subsequent evolution. During the first 50d, the decline in the $g-$band resembles those of the other SL-SNe Ic. But between 50-150d the decline rate changes markedly and the fading is slower. The reference template (164d) was used to retrieve the magnitudes after 71d. Because of the proximity of the template epoch and last SN epoch, we also used SDSS images as secondary template. The values retrieved with the two different templates were in agreement, strengthening simultaneously the lack of the SN at 145d and the detection of the faint host in the deep images of 164d.

3.1.5. SN 2012il

SN 2012il was discovered before it peaked in the $g-$ and $r-$bands. The first two epochs available are in the PS1 z_{P1}band and the CSS unfiltered system Drake et al. (2012). We can not set a robust constraint on the rise time for SN 2012il, but it is likely at least two weeks. The shape of the light curve around peak in $r-$band is possibly asymmetric as in PTF11rks and SN 2010gx, although we are somewhat constrained in this statement due to the uncertainty of the peak epoch. As for SN 2011ke, we see a clear change in the decline rate after 50 days, when SN 2012il has a slower decline (shown in Fig. 2. This change in decline to a slower fading rate is illustrated with the latest detection in all three filters riz at ~ 113d after peak. The reference template (327d) was used to retrieve the magnitudes at 113d and the g magnitudes after 58d.

3.2. Absolute Magnitudes

In calculating absolute magnitudes (and subsequently bolometric magnitudes), we have assumed negligible internal host galaxy reddening for all the objects, and applied only foreground reddening, with the values reported in Sect. 2. No Na ID absorption features due to gas in the hosts were observed. However, we can not exclude possible dust extinction from the hosts, therefore the absolute magnitudes reported here are technically lower limits. Given that the hosts are all dwarf galaxies, and the transients have quite blue spectra around peak it appears that any correction would be small. We computed k-corrections for each SN using the spectral sequence we have gathered. For photometric epochs for which no spectra were available, we determined a spectral energy distribution (SED) using the multi-color photometric measurements available. This SED was then used as a spectrum template to compute the K-corrections. Comparisons between the two methods (K-correction directly from spectra, or with the photometric colours) showed no significant differences. We also determined K-corrections for SN2010gx using the spectral method and using photometric colours. Again we found consistency between the two methods. After applying foreground reddening corrections and K-corrections we estimated absolute rest-frame peak magnitudes (cfr. Tab. 1).

In Fig. 3, we compare the rest frame $g-$band absolute light curves (in the AB system) of the SNe studied here with those of other low-z super-luminous events and the well studied Type Ic SN 1998bw (Galama et al. 1998; McKenzie & Schaefer 1999; Sollerman et al. 2000; Patat et al. 2001). The epochs of the maxima were computed with low-order polynomial fits and by comparison of the light curves and their colour evolution with those of other SL-SNe, and are listed in Tab. 1. The absolute peak magnitudes of PTF11rks and PTF10hgi are fainter than the bulk of SL-SNe, although they are still ~ 2 mag brighter than SN 1998bw. Interestingly, the two faintest SL-SNe Ic display different decline rates to each other, PTF11rks is similar to SN 2010gx whereas PTF10hgi decreases at a slower rate. The other three objects have peak magnitudes comparable with that of SN 2010gx ($M_g \approx -21.67$) and show a similar decline. The decline slope changes in four of the five objects after 50 days in the rest frame (while for the other, SN 2011ke, our data do not constrain it). The light curves then settle on a tail resembling the decay of ^{56}Co. This is apparent in Fig. 3 as the tails of the SL-SNe are similar to that of SN 1998bw which is known to be powered by ^{56}Ni. The light curves follow the ^{56}Co decay within errors of 10%, the biggest discrepancy is for SN 2011kf which falls more rapidly between 100-200 days. SN 2007bi (Gal-Yam et al. 2009; Young et al. 2010) also followed the ^{56}Co decay at late times, but with a tail that is ~ 2 mag brighter than the SL-SNe Ic, and with a
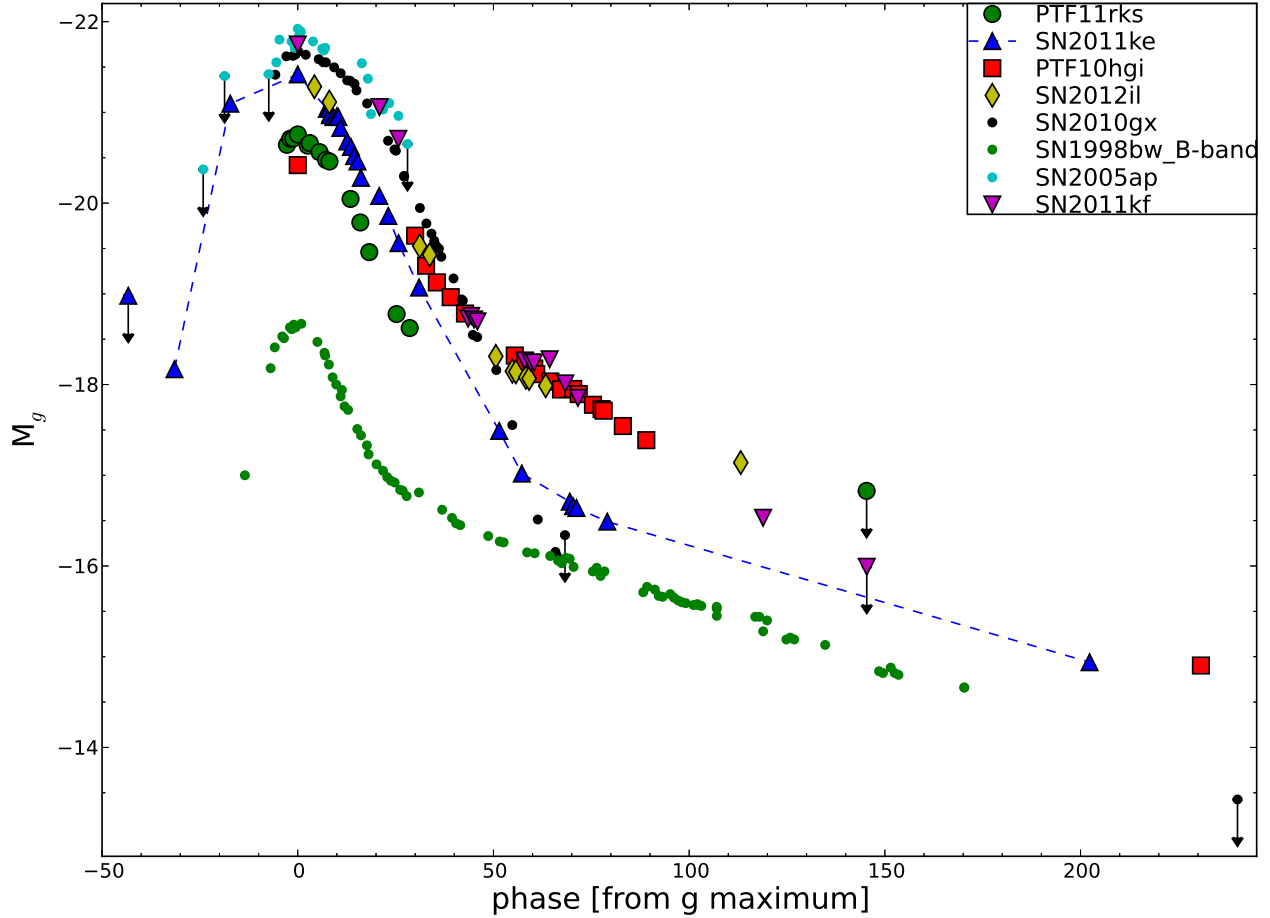
FIG. 3.— $g-$band absolute light curves of PTF11rks, SN 2011ke, PTF10hgi, SN 2011kf and SN 2012il and a number of super-luminous events as well as the stripped envelope SN 1998bw. The light curves for each SN have been derived by correcting the observed broadband photometry for time dilation, distance modulus, foreground extinction, and differences in effective rest-frame bandpass (K-correction). The last PTF10hgi and SN 2012il points were converted from the r mag applying a colour correction derived from SN 2011ke and SN 2011kf at similar epochs.

much slower overall evolution. We also note that the light curves of our objects flatten at slightly different epochs, with the tail for SN 2011ke commencing ~ 10 days after the last point in the lightcurve for SN 2010gx.

3.3. *Colour Evolution*

We computed rest-frame colour curves, after accounting for the reddening and redshift effects of time-dilation and $K-$correction. The colour curves are useful probes of the temperature evolution of the SNe. We also calculated rest-frame colour evolution of SN 2010gx, the only other SL-SN Ic with a good coverage in SDSS filters at a similar redshift. In Fig. 4 the SL-SNe show a constant colour close to $g - r = 0$ from the pre-peak phase to ~ 15d. This evolution is similar to the colour evolution of the higher redshift PS1-10ky in the observed bands $i_{\mathrm{P1}} - z_{\mathrm{P1}}$ Chomiuk et al. (2011). The constant colour until 15 d implies that the SED does not evolve over these epochs. Up to maximum light, the spectra of these SL-SNe appear to be blue, with the only strong features being the O II lines in this range covered by the gr filters (Pastorello et al. 2010; Quimby et al. 2011a;
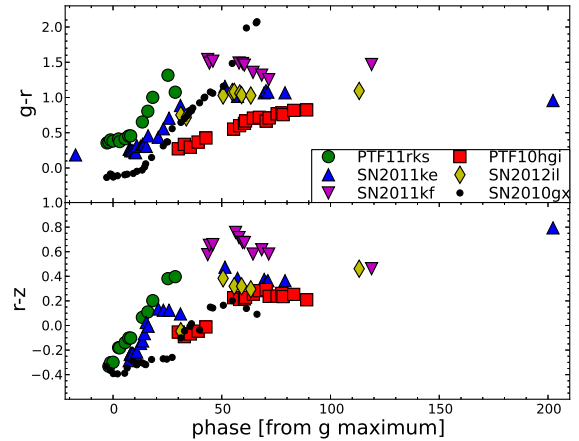

FIG. 4.— Comparison of the dereddened and $K-$corrected colour evolution. PTF11rks, SN 2011ke, SN 2012il, PTF10hgi and SN 2011kf are shown together with the well sampled SN 2010gx.

Chomiuk et al. 2011; Leloudas et al. 2012). Hence this could be due to an approximately constant temperature. This is also illustrated in Fig. 8 of Chomiuk et al.
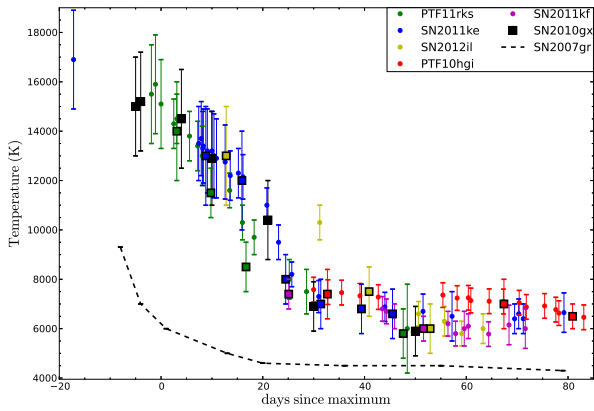
FIG. 5.— Evolution of the continuum temperature of PTF11rks (green), SN 2011ke (blue), SN 2012il (gold), PTF10hgi (red) and SN 2011kf (purple) are reported with those of SN 2010gx (black). The dashed black line shows the temperature evolution in the normal Type Ic SN 2007gr. Dots denote measurements from photometry, whereas squares are spectroscopic measurements.

(2011) for the higher redshift PS1-10ky. Close to peak the O II lines disappear, leaving the spectra featureless for ~ 10 days, while after peak the temperature begins to decrease (see Sect. 5.1). A monotonic temperature decline between 14000 K and 12000 K (blackbody peak 2100 Å $\lesssim \lambda \lesssim$ 2500 Å) in objects with featureless spectra does not strongly affect the colour evolution for $\lambda \gtrsim \lambda_{\mathrm{peak}}$, as the slopes of blackbodies at these two temperatures are quite similar. To detect differences in temperature between a 12000 K and a 14000 K blackbody requires colour curves which sample rest wavelengths below 3800 Å, such as the $g - z$ colour of PS1-10ky. And indeed this object did show an increase in $g - z$.

After this early period of constant colour, the $g - r$ colour increases, reaching another phase of almost constant value at ~ 40d, perhaps indicating a decrease in the cooling rate. There are some exceptions to this behaviour, as seen for PTF11rks and PTF10hgi. The $g - r$ colour of PTF11rks increases earlier and with a steeper slope than the other SNe, but unfortunately our data stop before the possible second period of constant colour. In contrast, the $g - r$ colour for PTF10hgi increases much more slowly, and only reaches the possible late constant phase at ~ 80d.

The $r - z$ colours of the sample show a roughly constant increase from peak to $\sim 50 - 60$d, when the colour evolution appears to flatten. The two exceptions are again PTF11rks and PTF10hgi; the former increases in $r - z$ more rapidly than the other objects, whereas the latter does not become as red, and experiences a clear decrease in $r - z$ after 80d. The $r - z$ colour evolution of SN 2010gx is similar to that of SN 2011ke and PTF10hgi.

3.4. *Temperature evolution*

In Fig. 5 the evolution of the temperature is plotted. This is derived from a blackbody fit to the continuum of our spectra (see Sect. 5), and compared to those of SN 2010gx and SN 2007gr. We also fit colour temperatures at rest-frame with a blackbody and the measurements are in good agreement with those from spectra.

Only PTF11rks has a good temperature coverage around peak, whereas our spectroscopic data are not well

sampled at that phase. While we can not clearly confirm the apparent constant temperature seen in SN 2010gx until ~ 10d, the epochs either side at ± 10d are suggestive of a roughly constant temperature phase. After ~ 10d a clear decline in temperature is seen, with a rate of decline of ~ 2500 K over 10d. This decline continues until the SN reaches a constant temperature of ~ 6000 K prior to, and during, the pseudo nebular phase.

4. BOLOMETRIC LUMINOSITY

Simultaneous UV–optical–NIR photometry at all epochs is required to obtain a direct measurement of the bolometric luminosity. This is typically difficult to attain at all epochs during a SN lightcurve, and we do not have complete wavelength coverage for the five SL-SNe. Nevertheless, valid corrections can be applied to the observed photometric bands to compute the bolometric flux.

The effective temperatures of the photospheres of SL-SNe Ic during their first 30-50 days after explosion are between $T_{\mathrm{bb}} \sim 13000 - 19000$ K (see Table 10 and Pastorello et al. 2010; Chomiuk et al. 2012). This means that their fluxes peak in the UV ($\lambda < 3000$ Å) during this period while our $griz$ bands typically cover from rest-frame 3800 Å redwards. Thus a significant fraction of the flux is not covered by the optical $griz$ imaging. At around 20d after peak, the effective temperatures tend to drop below 10000 K, hence the SEDs peak between 3000 Å and 4000 Å. Although the peak of the SED moves redward, a significant amount of the bolometric flux is radiated in the UV even during these late stages. In the following, we will use the term "$griz$-bolometric lightcurve" to refer to a bolometric lightcurve determined using only the specified filters (in this example, $griz$) with the flux set to zero outside the observed bands.

Initially, the broad band magnitudes in $griz$ were converted into fluxes at the effective filter wavelengths, then were corrected for the adopted extinctions (cfr. Sect. 2). A SED was then computed over the wavelengths covered and the flux under the SED was integrated assuming there was zero flux beyond the integration limits. Fluxes were then converted to luminosities using the distances previously adopted. We initially determined the points on the $griz$-bolometric lightcurves at epochs when $griz$ were available simultaneously (or very close in time). For epochs with coverage in less than the four filters we were able to estimate the $griz$-bolometric lightcuves. Magnitudes from the missing bands were generally estimated by interpolating the light curves using low-order polynomials between the nearest points in time. For some points this interpolation was not possible and we used one of two methods. The first was an extrapolation assuming constant colours from neighbouring epochs, the second was using colours from the other SL-SNe at similar epochs. For example, we used the latter method for the last point on the lightcurve for PTF10hgi. The $griz$-bolometric light curves estimated using this technique are plotted in the left panel of Fig. 6.

Useful Swift photometry for UV flux measurements exists for PTF11rks and SN 2011ke (see Table 11). Which allow us to compare the $griz$-bolometric light curves and the $UVgriz$-bolometric lightcurves (pseudo-bolometric hereafter), where the UV component is determined from the $uvw2$, $uvm2$ and $uvw1$ filters covering 1800-3000Å.
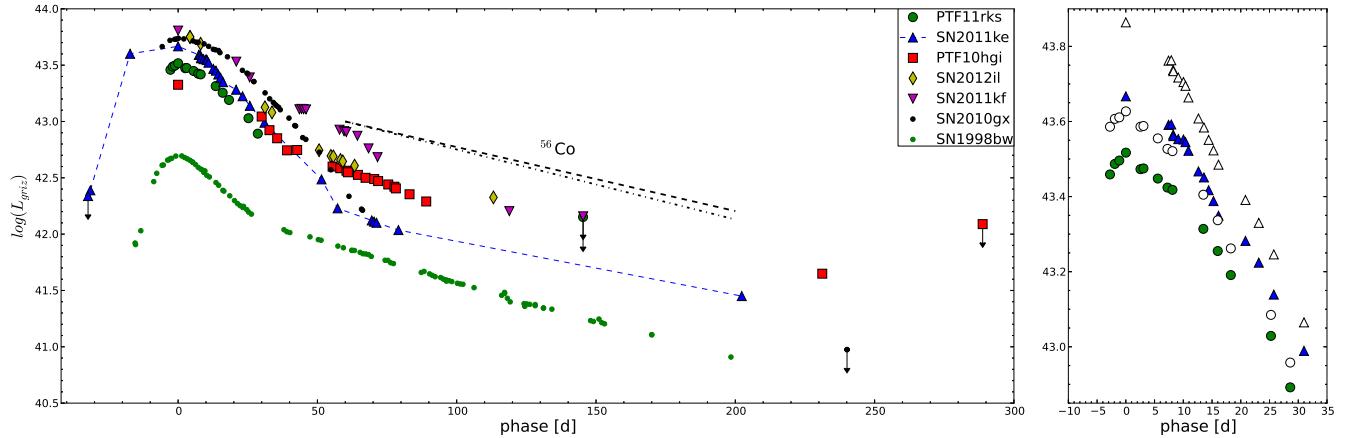
FIG. 6.— Left: *griz* bolometric lightcurves of PTF11rks, SN 2011ke, PTF10hgi, SN 2011kf, SN 2012il, SN2010gx and the Type Ic SN 1998bw (*BVRI* bolometric lightcurve). These bolometric lightcurves are computed after correcting the observed broadband photometry for time dilation and applying *K*-corrections. The dashed line is the slope of ^{56}Co to ^{56}Fe decay, the dot-dashed line is the decay slope with a 10% error. Right: Comparison between the *griz* bolometric light curve (filled symbols) and the *UVgriz* bolometric lightcurve of PTF11rks and SN 2011ke which include the measured UV flux from Swift photometry.
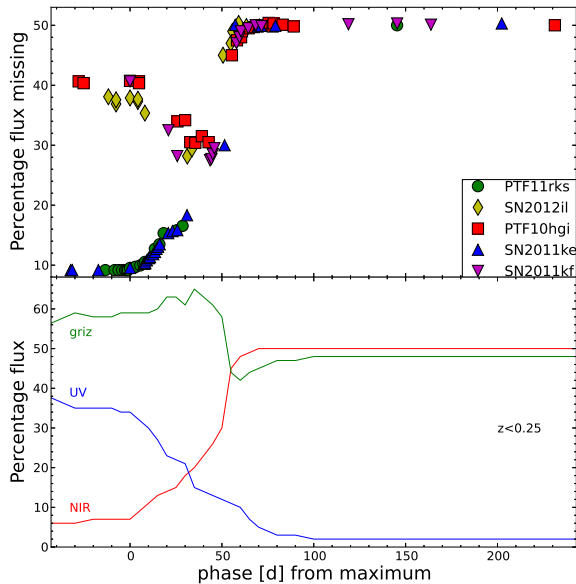

FIG. 7.— Top: Percentage of flux missed, assuming a black-body fit, in NIR by SN 2011ke and PTF11rks, and in UV+NIR by PTF10hgi, SN 2011kf and SN 2012il (the regions not covered by our photometry for each object). Bottom: Average percentage of the bolometric flux in UV (blue), optical (green) and NIR (red) for a representative SL-SN Ic at $z < 0.25$.

The difference between these two bolometric light curves, with and without the radiated energy below 3500 Å is shown in the right panel of Fig. 6.

Inclusion of the Swift photometry results in maximum luminosities for PTF11rks and SN 2011ke of L≈ 4.27×10^{43} erg s^{-1} and L≈ 7.08×10^{43} erg s^{-1} respectively. Hence the *griz*-bolometric fluxes, are a factor 1.5 lower than when including the 1800-3000Å range covered by $uvw1 - uvw2$ filters. While one could fit a black-body curve to the observed *griz* SEDs (or the spectra) and integrate under the curve to determine the emitted total flux across all wavelengths, this would not account for the strong line absorption shown in the rest-frame UV spectra (for example, clearly seen in the high-z objects

of Chomiuk et al. 2011). Hence from here on we will use *griz*-bolometric lightcurves for consistency on all objects, but we should bear in mind the additional contribution from the restframe UV that we have quantified in the right-hand panel of Fig. 6. The maximum luminosities reached by our computed *griz*-bolometric light curves are L$_{\text{PTF11rks}} \approx 3.24 \times 10^{43}$ erg s^{-1}, L$_{\text{SN2011ke}} \approx 4.47 \times 10^{43}$ erg s^{-1}, L$_{\text{SN2011kf}} \approx 6.45 \times 10^{43}$ erg s^{-1}, L$_{\text{SN2012il}} \gtrsim 4.47 \times 10^{43}$ erg s^{-1} and L$_{\text{PTF10hgi}} \approx 2.09 \times 10^{43}$ erg s^{-1}. As expected, these are lower than those reported by Chomiuk et al. (2011) for the $z \simeq 0.9$ objects PS1-10ky and PS1-10awh due to the lack of restrframe UV coverage for our low redshift sample.

The comparison in Fig. 6 further quantifies the large bolometric luminosities of these SL-SNe Ic - as discussed by Pastorello et al. (2010), Quimby et al. (2011a), Chomiuk et al. (2011) and Leloudas et al. (2012). There is clearly some diversity in the lightcurve peaks and widths. The low redshift of these objects makes it possible to follow the evolution beyond 100d after peak for the first time. Only one other object (SN 2010gx) has been investigated in this phase (Pastorello et al. 2010; Chen et al. 2013) and no detection was found at greater than 100 days. Quantifying the host contribution and using image subtraction to recover the SL-SN flux in these late phases is essential (as discussed in Sect. 3). It transpires that SL-SNe Ic show a large diversity in this phase, quite different to the relatively homogenous behaviour around peak. After 50d post maximum, all four of the SL-SNe Ic for which we have data (SN 2011ke, SN 2012il, SN 2011kf and PTF10hgi) show an abrupt change in the slope of the *griz*-bolometric lightcurve. The slope flattens and is quite similar to that of the decay of ^{56}Co to ^{56}Fe. SN 2011ke and PTF10hgi appear to decline even slower than the ^{56}Co slope.

Additionally, at these later phases we know from detailed coverage of CCSNe that a significant amount of radiation will be emitted in the near-infrared when the photospheric temperature drops below 10000 K. This flux can be, mostly, captured by *JHK* photometric observations. As we lack this complete wavelength coverage for our SL-SNe, we employed an SED method to deter-
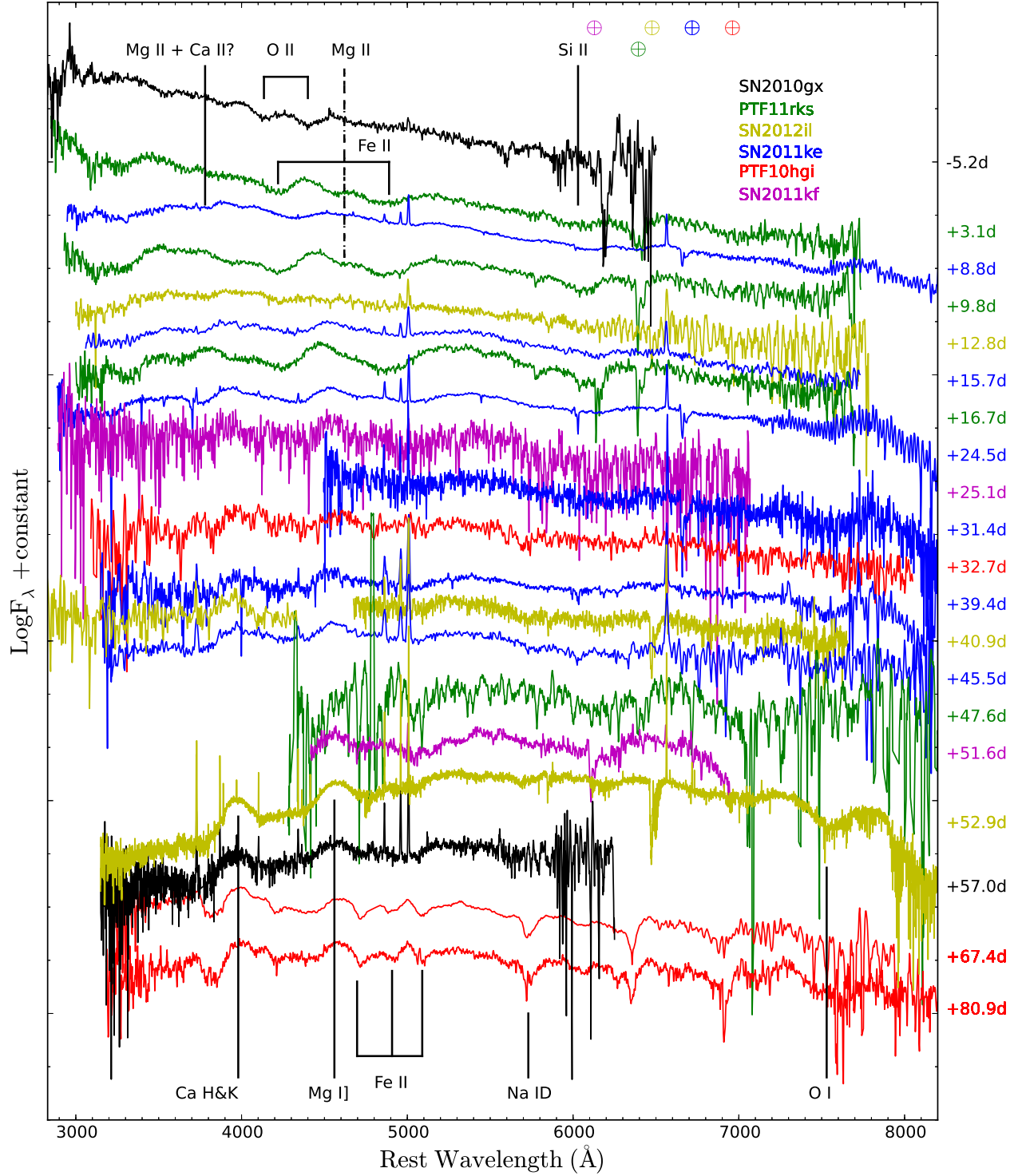
FIG. 8.— Spectra of PTF11rks are in green. SN 2011ke in blue, SN 2012il in gold, PTF10hgi in red, SN 2011kf in magenta and SN 2010gx (Pastorello et al. 2010) in black. The phase of each spectrum relative to light curve peak in the rest frame is shown on the right. The spectra are corrected for Galactic extinction and reported in the rest frames. The ⊕ symbols mark the positions of the strongest telluric absorptions. The most prominent features are labelled.

mine the correction. We use the photospheric temperatures (derived in Sec. 3.4) to derive simple blackbody SEDs and integrate the flux redwards of the rest-frame z-band. The flux missed in the NIR by our $griz$-bolometric measurements typically increases with time, and reaches roughly 50% after $\sim 60d$ post maximum. We plot the rest-frame NIR contributions as an average of all the SL-SNe presented here, for a representative redshift of $z < 0.25$, in the the bottom panel of Fig. 7. The optical component refers to the $griz$ bands (green line), and the NIR contribution beyond the z-band is denoted with the red line. We also used this method to have a secondary estimate of the UV contribution (blue line). In this case we integrated the flux under the black body spectra below the g-band. We compared the UV flux contribution with those evaluated from the two SNe which have Swift UV photometry and find the two are consistent within the errors. Fig. 7 summarises the flux contributions from the different wavelength regimes and allows the $griz$-bolometric lightcurves to be corrected when required.

If these tail phase luminosities were powered by ^{56}Co then it would require that there is full γ-ray trapping in the ejecta. This is not typically seen in Type Ic SNe. For example, the $BVRI$ bolometric lightcurve of SN 1998bw is shown for comparison which decays faster than the nominal ^{56}Co half-life. Sollerman et al. (2000) showed that if one assumes a fixed energy source (i.e. some mass of ^{56}Co), then the trapping efficiency decreases with time ($\propto t^{-2}$). Hence at the epochs of these SL-SNe (100-200 days) only around $\sim 45\%$ of the γ-rays would be trapped if they had similar ejecta mass and density profiles to other Type Ic SNe. This seems to be in contradiction to the measured slopes which appear either to follow the ^{56}Co decay timescale or even be slightly shallower. Despite this issue, we shall initially assume (for illustrative purposes) that the tail phases are actually powered solely by radioactive decay. This allows a corresponding mass of ^{56}Ni to be determined. Later in this paper we shall show that the tail phase luminosity may be powered by magnetar energy injection rather than ^{56}Co decay. Although four of the SL-SNe do show a flattening in their luminosity, it appears SN 2010gx does not, at least not at the detectability level of Chen et al. (2013). The data we have for PTF11rks does not allow a conclusion.

We initially make the assumption that γ-rays from ^{56}Co decay are fully thermalized during the full durations of the lightcurves we measure. We know that for typical SN Ic ejecta this is not the case, but it allows us to derive illustrative masses for ^{56}Co powering. The ^{56}Ni masses can thus be estimated using the formula

$$M(^{56}\text{Ni})_{\text{SN}} = 7.87 \times 10^{-44} L_t e^{\left[\frac{(t-t_0)/(1+z)-6.10}{111.26}\right]} M_\odot, \quad (1)$$

(e.g. as employed by Hamuy 2003), where t_0 is the explosion epoch, 6.1 d is the half-life of ^{56}Ni and 111.26 d is the e-folding time of the ^{56}Co decay, which release 1.71 MeV and 3.57 MeV, respectively as γ-rays (Woosley et al. 1989; Cappellaro et al. 1997).

This method gives ^{56}Ni masses of M(^{56}Ni)$_{\text{SN2011ke}} \sim$ 0.5 M$_\odot$, M(^{56}Ni)$_{\text{SN2012il}} \sim 1.2$ M$_\odot$, M(^{56}Ni)$_{\text{PTF10hgi}} \sim$ 1.1 M$_\odot$, while for SN 2011kf we retrieved an approximate M(^{56}Ni)$_{\text{SN2011kf}} \lesssim 1.9$ M$_\odot$. The measured de-

cline for SN 2011kf was slightly steeper than the fully trapped ^{56}Ni tail. We also estimated an upper limit M(^{56}Ni)$_{\text{PTF11rks}} \sim 1.3$ M$_\odot$, for PTF11rks based on the last epoch in which the SN was detected. These values should be considered as lower limits because of our limited rest frame wavelength coverage. At this phase, the contribution from the NIR plays an important role in the bolometric luminosity of SNe, as described above. Indeed, the SED of SN 1987A (data from Hamuy et al. 1988; Bouchet et al. 1989), also suggests that as much as 50% of the total flux for our transients could be outside the $griz$ bolometric lightcurves (at these epochs SN 1987A has already reached a constant temperature in the tail phase). Thus, to obtain a truer idea of the ^{56}Ni mass required to power these tail phases, the measured luminosities should be increased by roughly a factor two. In summary, we find that *if the luminosity in the tail phase is powered by ^{56}Co* then the ejected ^{56}Ni values required to power the lightcurves lie between 1.0 M$_\odot$ and 2.4 M$_\odot$, with an upper limit of 3.8 M$_\odot$ for SN 2011kf. These ^{56}Ni masses cannot power the peak of the lightcurves, as shown by Pastorello et al. (2010); Quimby et al. (2011a); Chomiuk et al. (2011); Leloudas et al. (2012). As we discuss below, we consider that the luminosity we detect in this phase is not necessarily due to radioactive ^{56}Co decay energy injection.

5. SPECTROSCOPY

All spectra were reduced (including trimming, overscan, bias correction and flat-fielding) using standard routines within IRAF. Optimal extraction of the spectra was adopted to improve the final signal-to-noise (S/N) ratio. Wavelength calibration was performed using spectra of comparison lamps acquired with the same configurations as the SN observations. Atmospheric extinction correction was based on tabulated extinction coefficients for each telescope site. Flux calibration was performed using spectro-photometric standard stars observed on the same nights with the same set-up as the SNe. The flux calibration was checked by comparison with the photometry, integrating the spectral flux transmitted by standard $griz$ filters and adjusted by a multiplicative factor when necessary. The resulting flux calibration is accurate to within 0.1 mag.

The collected spectra are shown in Fig. 8 together with spectra of SN 2010gx (Pastorello et al. 2010) for comparison. A version with all the spectra convolved to the same resolution and binned to the same pixel scale is shown in Appendix C. In our spectroscopic sample we do not have pre-peak spectral coverage, which typically shows C II, Si III and Mg II at UV wavelengths (< 3000Å) and O II in the optical region (Quimby et al. 2011a). The only lines which we may expect to be visible in our wavelength regions (namely O II) have already disappeared by $\sim 3 - 12$ days. At those epochs the SL-SNe spectra are featureless with the notable exception of PTF11rks, which shows weak broad absorption profiles of heavy elements such as Fe II, Mg II and Si II between 3000 Å and 6500 Å. A weak Ca II H&K absorption line is barely detected in PTF11rks, as is the case for SN 2011ke and SN 2012il. Redwards, Mg II $\lambda4481$ and the Fe II multiplet $\lambda\lambda4924, 5018, 5169$ are visible in PTF11rks. Other Fe II lines are barely visible in the region around 4500 Å, while

TABLE 2
Journal of spectroscopic observations.

Date	MJD	Phase[a] (days)	Range (Å)	Resolution[b] (Å)	Instrumental configuration
PTF11rks					
09/01/12	55936.36	3.1	3400-9200	13	NOT+ALFOSC+Gm4
17/01/12	55944.34	9.8	3500-9200	13	NOT+ALFOSC+Gm4
26/01/12	55952.57	16.7	3500-9200	13	NOT+ALFOSC+Gm4
03/03/12	55989.38	47.6	4300-8300	5	WHT+ISIS+R158R
SN 2011ke					
15/05/11	55696.52	8.8	3300-10000	14	TNG+DOLORES+LRB,LRR
22/05/11	55704.46	15.7	3400-9200	14	CAHA+CAFOS+b200
01/06/11	55714.48	24.5	3300-10000	14	TNG+DOLORES+LRB,LRR
09/06/11	55722.45	31.4	5100-9700	5	WHT+ISIS+R158R
18/06/11	55731.49	39.4	3300-10000	14	TNG+DOLORES+LRB,LRR
25/06/11	55738.49	45.5	3600-8800	16	NTT+EFOSC2+Gm13
SN 2012il					
30/01/12	55956.53	12.8	3400-9200	13	NOT+ALFOSC+Gm4
03/03/12	55989.51	40.9	5000-7800	5	WHT+ISIS+R300B,R158R
17/03/12	56003.56	52.9	3000-23000	2	VLT+XSHOOTER
PTF10hgi					
20/07/10	55398.41	32.7	3400-9200	14	CAHA+CAFOS+b200
28/08/10	55436.53	67.4	3200-8000	16	GEMINI+GMOS+R150
11/09/10	55451.37	80.9	3200-8300	10	WHT+ISIS+R300B,R158R
SN 2011kf					
30/01/12	55956.74	25.1	3400-9200	13	NOT+ALFOSC+Gm4
03/03/12	55989.75	51.6	4700-8300	10	WHT+ISIS+R158R

Note. — The telescope abbreviations are the same used in the Appendix, in Tabs. 5, 6, 7, 9 & 10 plus TNG = 3.6m Telescopio Nazionale Galileo + DOLORES; CAHA = 2.2m Telescope at Calar Alto Observatory + CAFOS; VLT = 8.2m ESO Very Large Telescope + XSHOOTER; GEMINI = 8.2m Gemini Telescope North + GMOS.
[a] phases with respect to the g-band maxima and corrected for time dilation
[b] FWHM of night sky emission lines

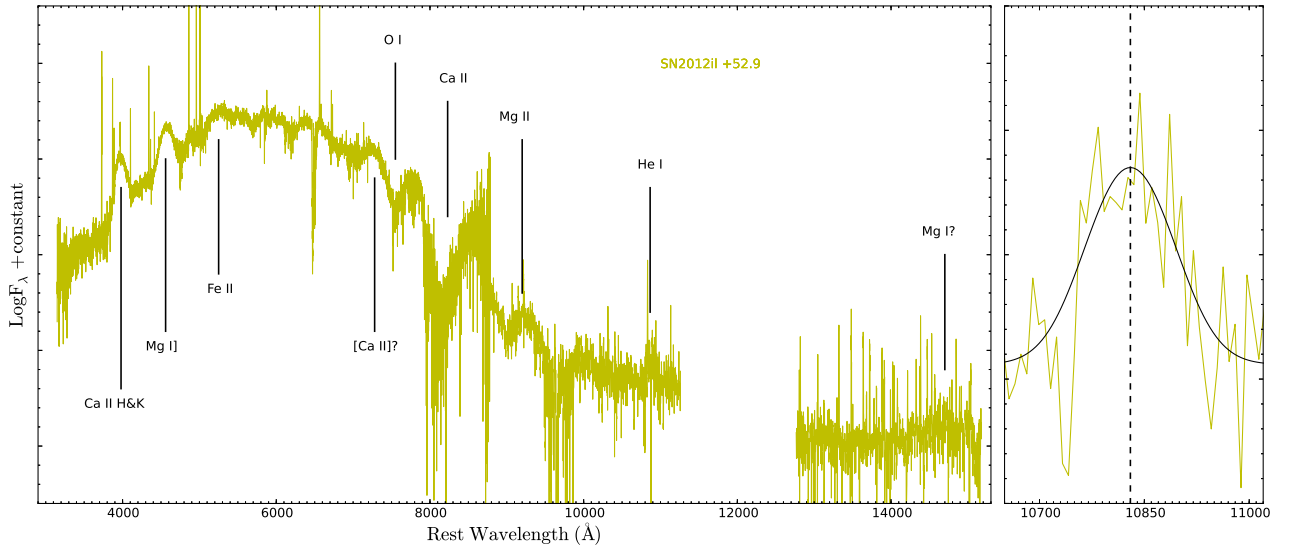

FIG. 9.— Spectrum of SN 2012il at ∼53d post maximum. The spectrum is corrected for Galactic extinction and reported in its rest frame. The most prominent features are labelled. In the right panel a zoom of the He I line (spectrum binned by a factor 10) is shown with the gaussian fit of the line. The dashed vertical line marks the expected position of He I λ10830.

a shallow absorption due to Si II λ6347 is also present. None of these lines are clearly detectable in SN 2011ke and SN 2012il at a similar phase.

Two weeks after maximum, SN 2011ke shows Mg II, Fe II and Si II lines together with a clearer Ca II feature, albeit still shallower than for PTF11rks. The spectra obtained around 30d for SN 2011kf and PTF10hgi have a low signal to noise (S/N) ratio of ∼ 10 which makes line analysis problematic. However, the comparison with the other spectra indicates broad absorption profiles from Mg II and Fe II. The only line visible in the red part of the spectrum (> 7000Å) is O I λ7775 in SN 2011ke.

From ∼ 30d after maximum onwards there is no strong evidence of new broad features emerging blueward of 8000Å, with the exception of the rise of Mg I] λ4571. The absorption lines of Mg and Fe become shallower, resulting in the emission components becoming more prominent from ∼50d onwards. The Fe II emission line at ∼ 5200 Å is broader than Mg I] suggesting it may be a blend. The only exception to this general trend is PTF10hgi. In the last two available spectra PTF10hgi shows Ca II H&K (possibly blended with Mg II), three distinct absorptions related to the individual components of the Fe II multiplet (λλ4924, 5018, 5169) and Na I D λλ5890,5896. Although the spectral evolution is relatively homogeneous, two of the sample have noticeable differences. In the first two weeks of evolution of PTF11rks the absorption line strengths look stronger, with $\overline{EW}_{PTF11rks} \sim 4 \times \overline{EW}_{SL-SNeIc}$. The later phase line formation in PTF10hgi also looks different, with narrower absorption lines more similar to velocities seen in Type Ic SNe (see the comparison with SN 2007gr in Fig.10) Weak, narrow emission lines (Hα, Hβ and [O III] λ4959, λ5007) from the host galaxies are also visible in all spectra, except those of PTF10hgi. These will allow metallicity and star formation rate measurements in the host, which is underway in a companion paper (Chen et al., in prep).

Fig. 9 shows the complete spectrum of SN 2012il taken at ∼ 53d with VLT+XShooter, which has the widest wavelength coverage for a SL-SNe obtained to date. As previously mentioned, bluewards of 8000 Å, Ca II H&K, Mg I], shallow Fe II and O I are present. A strong Ca II NIR triplet λλ8498, 8542, 8662 is visible, with the bulk of the absorption component at $v = 12000 \pm 2500 \, \mathrm{km \, s^{-1}}$. This is higher than the other absorption components (e.g. O I $v \sim 9500 \, \mathrm{km \, s^{-1}}$) and comparable with the velocities of the broad emission components of Ca II H&K, Mg I]. At about 7300Å a weak emission line is evolving and we tentatively identify it as [Ca II] λλ7291,7324 emission feature. The presence of [Ca II] and the emission lines around 4500 Å imply that the SNe is evolving, slowly, toward the nebular phase. This seems to coincide with the change in slope of the light curve. In the NIR the S/N∼5 in the continuum is less than in the optical (S/N∼30), although it is still adequate to identify the strongest lines. We identify Mg II around 9200 Å and Mg I λ15024, although the last identification is less certain due to the low S/N and the proximity of a strong telluric feature. Most significantly, we identify He I λ10830, the first sign of the presence of He in this group of SL-SNe Ic. We note that the only other ions which have transitions at this wavelength are Ar II, Fe I, Si I and C I. These are
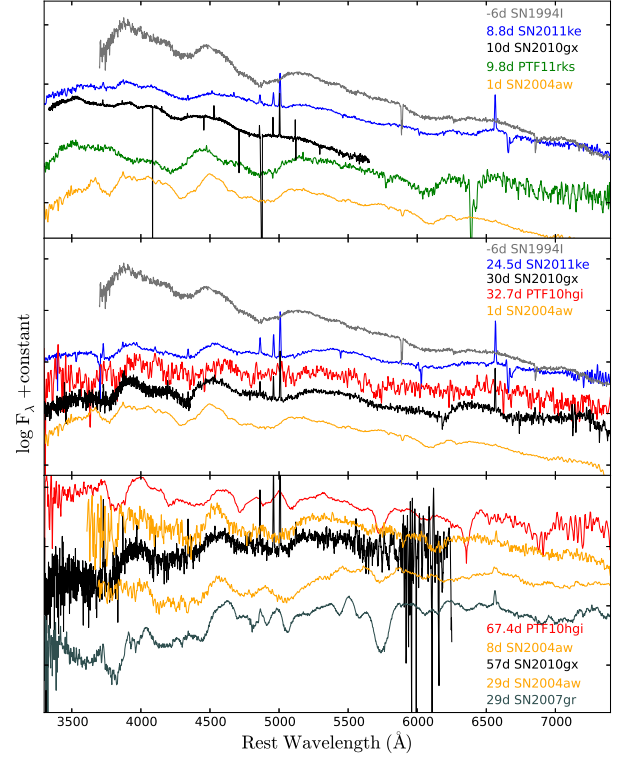

FIG. 10.— Top: comparison of early-time spectra of SN 2011ke and PTF11rks with that of SN 2010gx (Pastorello et al. 2010) and those of Type Ic SNe 2004aw (Taubenberger et al. 2006) and 1994I (Baron et al. 1996). At ∼10d post maximum PTF11rks is already more developed than SN 2011ke and SN 2010gx. Middle: comparison at about ∼ 30d post peak of the same objects as for the previous panel, but showing PTF11rks instead of PTF10hgi. Bottom: comparison of the spectrum of PTF10hgi at ∼ 67d with those of SN 2010gx at the pseudo nebular phase, SN 2004aw at maximum light during the photospheric period, and Type Ic SN 2007gr (Valenti et al. 2008; Hunter et al. 2009). The spectrum of PTF10hgi is more similar to those of SNe 2004aw and 2007gr at 29d rather than those of SN 2010gx at 57d and SN 2004aw at 8d (as noted in Pastorello et al. 2010).

expected to be intrinsically weaker than He I. There are no strong sky lines at the observed postion of this line ∼ 12725Å. Although we do not see other He I lines in the spectrum, this is not unexpected. In the Case B recombination in the temperature regime $T < 10000$ K and electron density $10^2 \leq n_e \leq 10^6$ - the λ10830 line is expected to be stronger than λ5876 line (the strongest in the optical region) by a factor 2 to 10.

The spectral evolution of the SL-SNe sample in this paper, provides additional information to that reported in Pastorello et al. (2010). In the top panel of Fig. 10 the comparison of the early time spectra with those of SN 2010gx (Pastorello et al. 2010), and the Type Ic SNe 1994I (Baron et al. 1996) and 2004aw (Taubenberger et al. 2006) highlights a difference in the line evolution between PTF11rks and other SL-SNe. The spectrum at 9.8d is similar to that of a Type Ic close to maximum light showing a faster transition to a Type Ic SNe than the others. In contrast, other SL-SNe such as SN 2011ke match normal Type Ic SNe only after ∼30d (middle panel Fig. 10), resembling the spectral transition of SN 2010gx at this epoch. This makes the temporal evolution of PTF11rks very similar to those of canonical
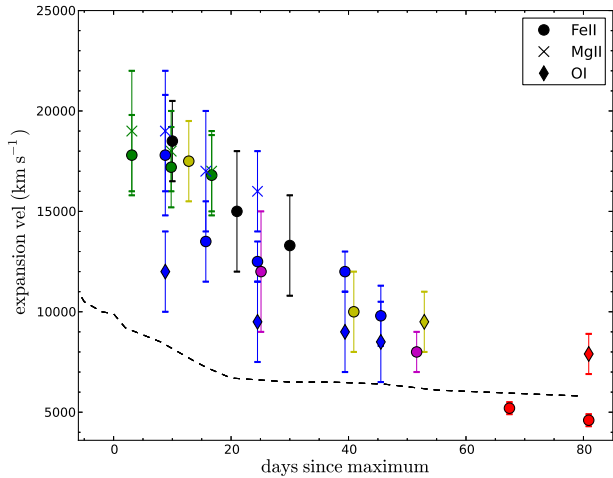
FIG. 11.— Expansion, photospheric velocity as measured from the different lines. Phases are relative to light curve peak. Measurements of PTF11rks (green), SN 2011ke (blue), SN 2012il (gold), PTF10hgi (red) and SN 2011kf (purple) are reported with those of SN 2010gx (black). The dashed black line shows the Fe II evolution in the normal Type Ic SN 2007gr.

SNe Ic. Again the low S/N of the spectrum of PTF10hgi (32.7d) precludes a precise analysis, although there are hints of a peculiar line evolution at wavelengths redder than 5500 Å. In the bottom panel, SN 2010gx resembles SN 2004aw at ~ 10d after peak whereas PTF10hgi matches normal Type Ic SNe at $\sim$30d, with a good match to SN 2007gr. From this comparison it appears that PTF11rks and PTF10hgi evolve to into Type Ic SN on timescales of about 20 days quicker than other SL-SNe. The "fainter" luminosity (M> −21) of these two objects and their faster evolution to Type Ic SNe may provide another clue to understand the evolutionary path of these transients. It appears from these objects that the lower the peak luminosity, the faster the evolution of the photospheric spectra, with a time delay of 10 days to the Type Ic phase instead of the usual 30 days shown by most SL-SNe Ic.

5.1. Expansion velocity

The expansion velocities measured for PTF11rks, SN 2011ke, SN 2012il, PTF10hgi and SN 2011kf are reported in Tab. 3, and are compared with those of SN 2010gx and the standard Type Ic SN 2007gr (Hunter et al. 2009) in Fig. 11. In the photospheric phase these were derived from the minima of the P-Cygni profiles and their errors were established from the scatter between several independent measurements. During the phase in which the objects appear to be transitioning to the nebular phase (i.e. beyond about 50 days) the velocities were computed as the FWHM of the emission lines (we will call this the pseudo-nebular phase). These are not tracers of the photospheric velocity and are reported for completeness; they will be discussed further in Sect. 6.2. We used Fe II $\lambda5169$, Mg II $\lambda4481$ and O I $\lambda7775$ to measure velocities during the photospheric phase, and Ca II H&K and Mg I] $\lambda4571$ during the pseudo-nebular phase. The Fe II velocity evolution monotonically declines for all transients, ranging from ~ 18000 km s^{-1} around peak to ~ 8000 km s^{-1} at 50d. After this epoch we have only PTF10hgi spectra, and they still show clear absorption components

of Fe II. The decline in velocity is faster and it reaches ~ 4600 km s^{-1} at the last epoch of 80 days, which is quite similar to the Fe II velocity of SN 2007gr. Mg II in the photospheric phase is always seen at higher velocity than Fe II, and decreases linearly by ~ 1000 km s^{-1} every 10 days. The O I velocity is comparable with that of Fe II, with the exception of SN 2011ke where it is slower than all other ions (albeit with large uncertainties due to the low S/N). Ca II and Mg I] appear after $\sim$40d from maximum light and show the same intensity and velocity of ~ 11000 km s^{-1} in the entire sample.

The PTF10hgi spectra after 60d show Ca II absorption at late epochs, similar to normal Type Ic SNe. Fig. 11 shows evidence for decreasing line velocity with time, especially from 10d post peak as seen for SN 2010gx (previously reported as a comparison in Chomiuk et al. 2011). Our analysis shows a clear sign of change in the rate of photospheric expansion $(30 − 40$d$)$, with a decline which resembles that typically observed during the photospheric phase of a CCSN explosion.

6. ON THE NATURE OF SL-SNE IC

The SN sample presented in this paper provides new data for understanding the nature of super-luminous events. The similarity within this family is well established: high luminosity, similar spectral evolution and an origin in faint host galaxies. The overall spectral evolution is indeed similar to that of SNe Ib/c, although SL-SNe spectroscopically evolve on a much longer timescale. However, the observed parameters of SL-SNe present several problems in interpreting the explosion. The enormous luminosity at peak cannot be powered by radioactive ^{56}Ni (Pastorello et al. 2010; Quimby et al. 2011a; Chomiuk et al. 2011; Leloudas et al. 2012) which is the canonical energy source for SNe Ic emission. However, we showed in Section 4 that the tail phase luminosity in some objects declines in a similar fashion as to what would be expected from ^{56}Co decay.

In the following subsections we use this most extensive dataset to constrain plausible models for the origin of these SNe, particularly using the bolometric luminosity from -30 to 200d and the temperature and velocity information. In this paper we focus on quantitative modeling of the magnetar spin down scenario (Sect. 6.2). Several other models have been proposed, which we briefly review in Sect. 6.1. The bolometric light curves used in this Section are corrected for flux missed in *both* UV and NIR as described in Section 4.

6.1. Alternative models

Alternative models have been proposed: the spin down of a rapidly rotating young magnetar (Kasen & Bildsten 2010; Woosley 2010; Dessart et al. 2012); interaction of the SN ejecta with a massive (3-5 M$_\odot$) C/O-rich circumstellar medium (CSM, Blinnikov & Sorokina 2010) ; shock breakout from dense mass loss (Chevalier & Irwin 2011); or pulsational pair instability in which collisions between high velocity shells are the source of multiple, bright optical transients (Woosley et al. 2007). The first scenario considered is the pulsational pairinstability model, where the luminosity is powered by the collision of shells of material ejected at different times by the pulsations (see Chatzopoulos & Wheeler 2012, for the implementation of this on SL-SNe Ic). The outbursts

TABLE 3

Observed blackbody temperature, expansion photospheric velocities from Fe ii λ5169, Mg ii λ4481 and O i λ7775 in our SL-SNe sample on the left. Expansion velocities from Ca ii H&K and Mg i] λ4571 on the right.

Date	MJD	phase[a] (days)	T (K)	v (Fe II) (km s^{-1})	v (Mg II) (km s^{-1})	v (O I) (km s^{-1})	v (Ca II) (km s^{-1})	v (Mg I]) (km s^{-1})
				PTF11rks				
09/01/12	55936.36	3.1	14000 ± 2000	17800 ± 2000	19000 ± 3000			
17/01/12	55944.34	9.8	11500 ± 1000	17200 ± 2000	18000 ± 2000			
26/01/12	55952.57	16.7	8500 ± 1000	16800 ± 2000	17000 ± 2000			
03/03/12	55989.38	47.6	5800 ± 1000					
				SN 2011ke				
15/05/11	55696.52	8.8	13000 ± 2000	17800 ± 3000	19000 ± 3000	12000 ± 2000		
22/05/11	55704.46	15.7	12000 ± 2000	13500 ± 2000	17000 ± 3000			
01/06/11	55714.48	24.5	8000 ± 1000	12500 ± 1000	16000 ± 2000	9500 ± 2000		
09/06/11	55722.45	31.4	7000 ± 1000					
18/06/11	55731.49	39.4	6800 ± 1000	12000 ± 1000		9000 ± 2000		10000 ± 1500
25/06/11	55738.49	45.5	6600 ± 1000	9800 ± 1500		8500 ± 2000	10000 ± 1500	10000 ± 1500
				SN 2012il				
30/01/12	55956.53	12.8	13000 ± 2000	17500 ± 2000				
03/03/12	55989.51	40.9	7500 ± 1000	10000 ± 2000				
17/03/12	56003.56	52.9	6000 ± 1000			9500 ± 1500	12000 ± 2500	12000 ± 2500
				PTF10hgi				
20/07/10	55398.41	32.7	7400 ± 1000					
28/08/10	55436.53	67.4	7000 ± 1000	5200 ± 300			8300 ± 800	9800 ± 1000
11/09/10	55451.37	80.9	6500 ± 500	4600 ± 300		7900 ± 1000	8000 ± 800	9500 ± 1000
				SN 2011kf				
30/01/12	55956.74	25.1	7400 ± 1000	12000 ± 3000				
03/03/12	55989.75	51.6	6000 ± 1000	8000 ± 1000				

[a] corrected for time dilation

are expected to be energetic, reaching very high peak luminosities and creating hot ($T_{eff} \approx 25000$ K), optically thick photospheres (Woosley et al. 2007). PS1 has occasionally observed the explosion sites of the five SL-SNe presented here, and SN 2010gx on 3-5 occasions (per event) in one of $g_{P1}r_{P1}i_{P1}z_{P1}y_{P1}$ filters, reaching typical AB magnitudes of 22, 21.6, 21.7, 21.4, 19.3 (see Sect.2). This would correspond to absolute magnitudes of roughly -16 to -19. We found no detection of any previous outburst to these magnitude limits in the 1-2 year periods before explosion. Typically there were 5-10 epochs of images from PS1. This is not a constant monitoring period, and it does not rule out that pre-explosion outbursts occur, but we have found no evidence for them.

The second scenario is that of circumstellar interaction proposed by Chevalier & Irwin (2011) in which the interaction between the ejecta and the CSM converts the ejecta's kinetic energy into radiation. This requires the diffusion radius of the SN to be about the radius of the stellar wind expelled by the SN progenitor. Based on this model of Chevalier & Irwin (2011), Chomiuk et al. (2011) determined the dense wind and ejecta parameters for the observed $z \simeq 1$ SL-SNe. This requires a mass-loss rate of 6 $M_{\odot}$ in the last year before the SN explosion, with an outer radius of around 40000 $R_{\odot}$, and ejecta mass of 10 $M_{\odot}$ (consistent with the estimates reported in Moriya & Tominaga 2012). The rise times of our low-z SNe are similar to that of PS1-10awh (from Chomiuk et al. 2011) - around 10-30 days which would lead to similar estimates of masses. The detection of He i

in SN 2012il at $\sim$ 53d is perhaps some hint that the dense CSM wind could be plausible, since it is difficult to find any known massive star example in the Local Universe which has a dense and extended wind comprising 6 $M_{\odot}$ of C+O material only. Although the S/N in the NIR is low, the He i line is relatively broad, indicating that it arises from ejecta. Although most SL-SNe have similar rise times which are feasible in the diffusion model of Chevalier & Irwin (2011), the light curves of SN 2010gx (Pastorello et al. 2010), PTF11rks and SN 2012il are not symmetric, which one would expect in this dense wind scenario. However, Ginzburg & Balberg (2012) showed as the rise and fall times can be different. They also showed that the tail phase can be explained as diffusion from the inner layers which can slow the decline. We have not investigated in this scenario in depth, but a combination of this model plus a ^{56}Ni tail would be unlikely because of the necessity of full γ-ray trapping (see Sec. 4).

A variant of the previous scenario was proposed by Blinnikov & Sorokina (2010) claiming high luminosities from a radiative shock in a massive C-O shell. The shells have radii and density profiles that are similar to the dense wind of Chevalier & Irwin (2011), with a density gradient of $\rho(r) \propto r^{-1.8}$ and radii of the order 10^5 $R_{\odot}$. Considering a total ejecta mass $M_{ej} \lesssim 1$ $M_{\odot}$, which collides with a shell of mass 5 $M_{\odot}$, these models have initial energies ($2-4 \times 10^{51}$ erg) higher than those retrieved by the expansion velocities during the pseudo nebular phase in our set of spectra ($\sim 1 \times 10^{51}$ erg). Moreover, the light
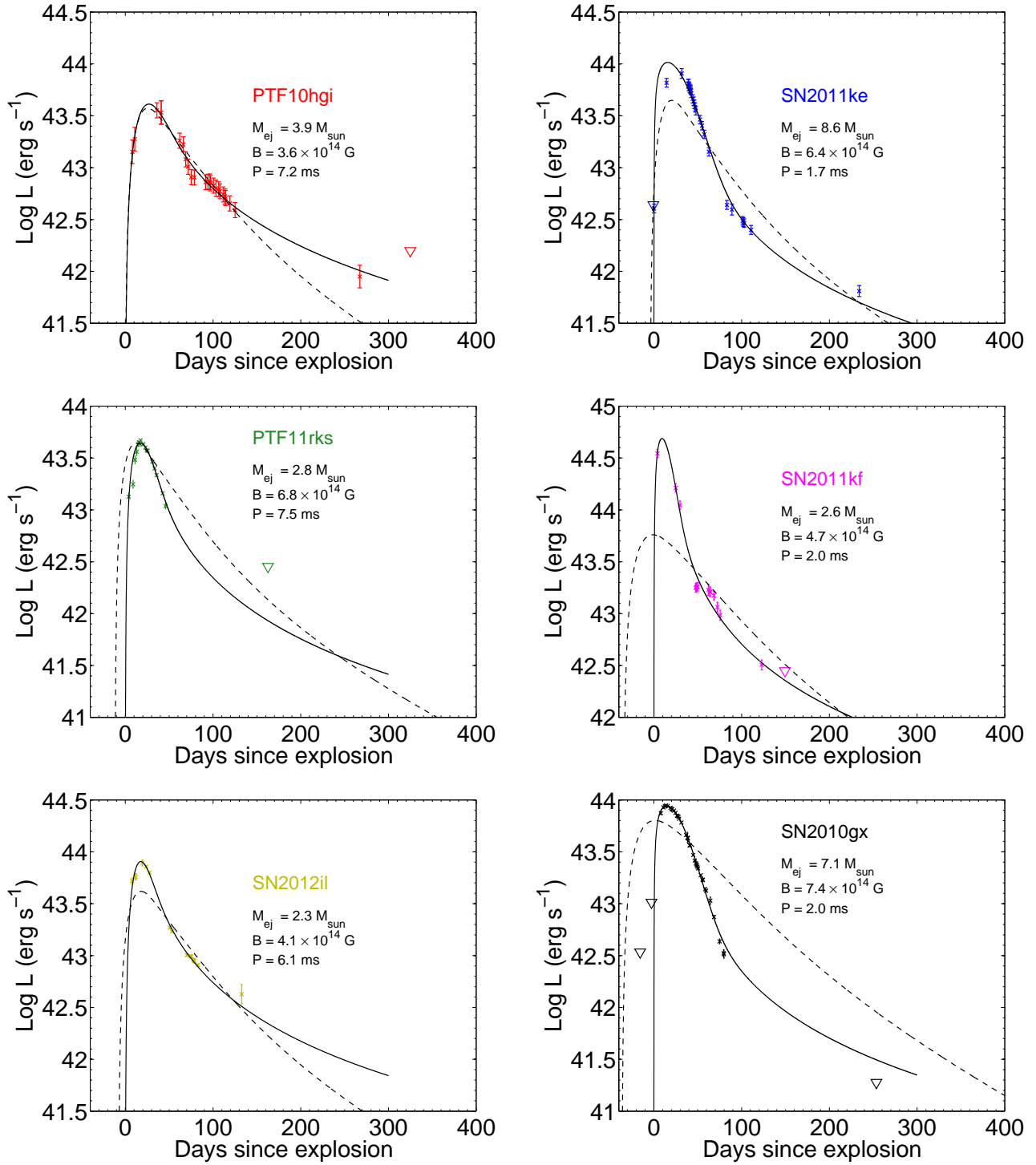
Fɪɢ. 12.— The bolometric light curves of PTF10hgi, SN 2011ke, PTF11rks, SN 2011kf, SN 2012il and SN 2010gx and the diffusion semi-analytical model that best fit the light curve (black solid line). Limits are shown as empty upside down triangles. Best fit of the ^{56}Ni model (black dashed line) for each SN is also reported. The x-axes refer to magnetar models.

curves are too shallow and they are not able to reproduce the SN 2010gx decline after 30d post maximum light. We find no unequivocal signs of interaction in the spectra of the objects.

In Sects. 3.1 and 4 we have presented detections of the SNe at later times than published to date, due to our focus on low redshift candidates. We detect a flattening of the lightcurve and a tail phase in four out of five transients and this slope appears to be consistent with ^{56}Co decay. In summary these interaction scenarios can reproduce the peak energy and diffusion time. However the ejecta/shell velocity should be lower (by about a factor of 2) than those observed. And one still needs another power source for the late time luminosity that we now detect in these SL-SNe Ic.

As shown previously by Chatzopoulos et al. (2009); Pastorello et al. (2010); Quimby et al. (2011a); Chomiuk et al. (2011); Chatzopoulos et al. (2012); Leloudas et al. (2012), the lightcurve peaks cannot be fit with a physically plausible ^{56}Ni diffusion model like normal SNe Ic, and our similarly shaped lighcurves result in the same conclusion. If the tail phase was actually due to ^{56}Co powering, then approximately 1-4 M$_\odot$ of ^{56}Ni would be required. But this would not be enough to power the peak luminosity solely through radioactive heating. In Fig. 12 we also show the best fitting ^{56}Ni-powered models, under the assumptions that the ^{56}Ni mass must be <50% ejecta mass, and that the ejecta velocities are less than 15000 km s^{-1}. The first assumption is based on the implausibility of a pure ^{56}Ni ejecta; Umeda & Nomoto (2008) found typical ^{56}Ni masses which are at most 20% of the ejecta, while if the ejecta was comprised of more ^{56}Ni than this, we would expect to see spectra dominated by Fe-group rather than intermediate mass elements. The velocity constraint is motivated by the observed velocities in our sample. Thus we derived kinetic energies of $6.2 \lesssim E(10^{51}\text{erg}) \lesssim 15.0$, ejecta masses of $5.9 \lesssim M_{\text{ej}}(\text{M}_\odot) \lesssim 13.0$ and ^{56}Ni masses of $2.9 \lesssim M_{^{56}\text{Ni}}(\text{M}_\odot) \lesssim 6.0$ (see Appendix D.5 for further details). From the fits appear that no physical and consistent solutions for ^{56}Ni heating can be determined, as found by previous authors (Pastorello et al. 2010; Quimby et al. 2011a; Chomiuk et al. 2011; Leloudas et al. 2012). One could invoke a combination of CSM interaction to explain the peak luminosity and then ^{56}Ni masses of 1-4 M$_\odot$ to account for the tail phases. But as discussed above, this requires full γ-ray trapping and somewhat fine tuning of the two scenarios to work in unison.

6.2. Magnetar model

Kasen & Bildsten (2010); Woosley (2010); Dessart et al. (2012) have already proposed that a rapidly spinning magnetar can deposit its rotational energy into a supernova explosion and significantly enhance the luminosity. This appears to be an appealing scenario as the model is fairly simple, and this additional power source can potentially transform a canonical Type Ic SN into a SL-SN Ic. To investigate this further and quantitatively compare our extensive lightcurves with this model we have derived a semi-analytical diffusion models. We use standard diffusion equations derived by Arnett (1982) and add magnetar powering (as in

Fig. 13.— Left: photospheric velocities of SN 2011ke, PTF11rks, SN 2012il, PTF10hgi, SN 2011kf, SN 2010gx and and their values in the semi-analytical models best fitting the light curve data. Different symbols correspond to different ions as in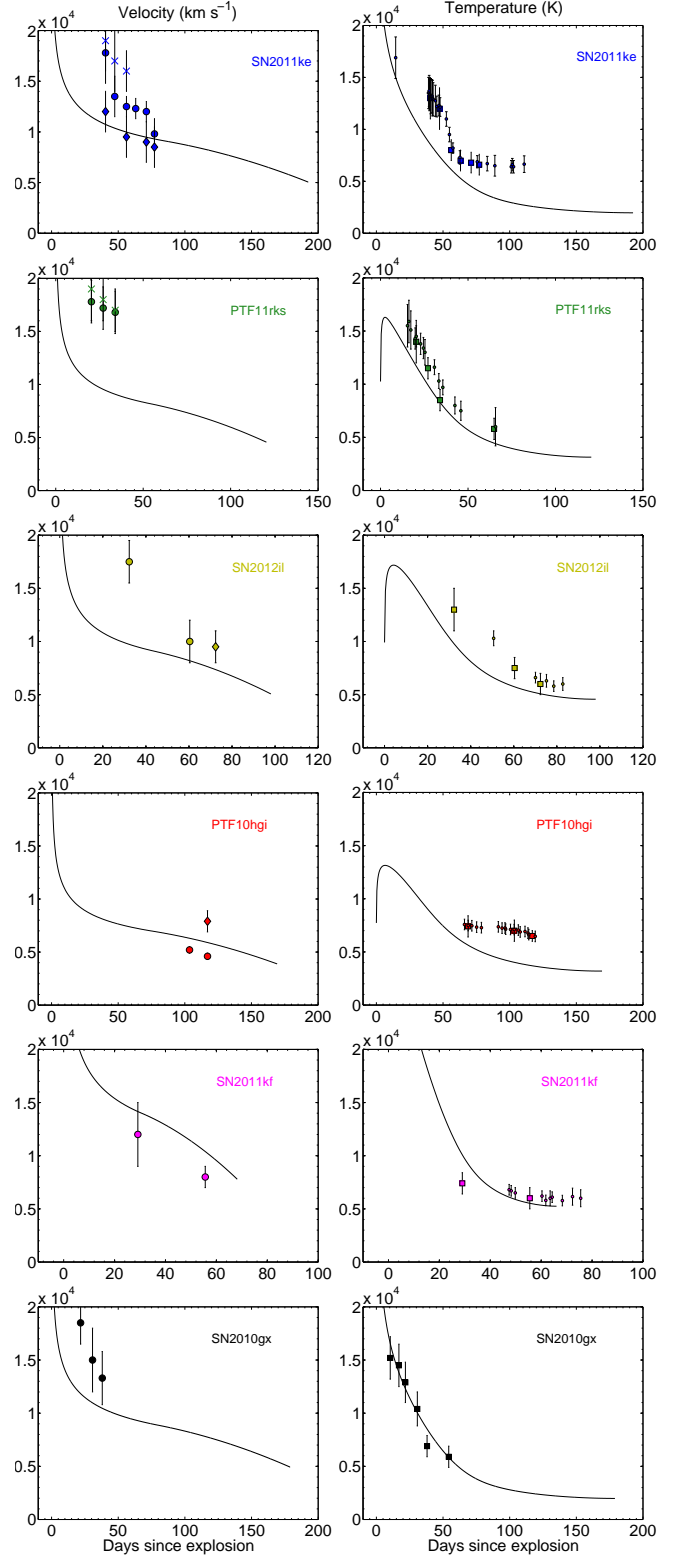 Fig. 11 Right: temperature evolution of SN 2011ke, PTF11rks, SN 2012il, PTF10hgi, SN 2011kf, SN 2010gx and their values in the semi-analytical models best fitting the light curve data.

Kasen & Bildsten 2010) to fit the light curves of our five objects. A full description can be found in Appendix D. Assuming full trapping of the magnetar radiation[18], the ejecta mass $M_{\rm ej}$, explosion energy $E_{\rm k}$, and the opacity κ only influence the bolometric light curve through their combined effect on the diffusion time-scale parameter (see Appendix D)

$$\tau_{\rm m} = 10\,{\rm d} \left(\frac{M_{\rm ej}}{1\,M_\odot}\right)^{3/4} \left(\frac{E_{\rm k}}{10^{51}\,{\rm erg}}\right)^{-1/4} \left(\frac{\kappa}{0.1\,{\rm cm}^2{\rm g}^{-1}}\right)^{1/2}.$$
$$(2)$$

The magnetar luminosity depends on two parameters, the magnetic field strength B_{14} (expressed in terms of 10^{14}G) and the initial spin period $P_{\rm ms}$ (in milliseconds). Combined with the explosion date t_0, we therefore have four free parameters to fit. Tab. 4 lists the best-fit parameters for each object, and Fig. 12 shows the fits. As the χ^2 fitting gives good matches to models *without* ^{56}Ni, we have no need to introduce ^{56}Ni as an additional free parameter. All the models have M(^{56}Ni) $= 0\ M_\odot$ and we investigated the sensitivity to the assumed ^{56}Ni mass by recomputing the fits including 0.1 $M_\odot$ of ^{56}Ni in the ejecta (the typical ^{56}Ni yield in core collapse SNe). We find virtually the same fit parameters as we do without the nickel. As can be seen from Fig. 14 (top), the two magnetar models ($B_{14} = 5$, $P_{\rm ms} = 5$, $M_{\rm ej} = 5\ M_\odot$) with (red dashed) and without ^{56}Ni (black solid) are similar. The late decline rate in the magnetar model ($>$100d) is actually quite similar to the ^{56}Co decay rate as shown in Fig. 14 (bottom), but fully trapped γ-rays are required. As Fig. 14 shows, this full trapping is different from the typical light curve of a radioactivity-powered Type Ib/c SN in which full trapping is not observed. Recently, Dexter & Kasen (2012) showed that fall-back accretion can give a similar asymptotic behaviour of the light curve ($L_{\rm t} \propto t^{-5/3}$) which is a scenario that would need further investigation.

The lightcurves are quite well reproduced with appropriate choices of parameters, and the tail phase luminosities that we measure can also be explained with this model. The diffusion time scale parameters are between 15-35 days, which corresponds to ejecta masses of 2-9 $M_\odot$ for $\kappa = 0.1$ cm^2 g^{-1} (see Appendix D for further details about κ) and

$$E_{\rm k} = 10^{51} + \frac{1}{2}\left(E^{\rm mag} - E^{\rm rad}\right)({\rm erg}) \qquad (3)$$

where $E^{\rm mag}$ is the total energy of the magnetar and $E^{\rm rad}$ is the total radiated energy of the SN. We use a factor of 1/2 for an approximation of the average kinetic energy over the magnetar energy input phase, which we show in the Appendix D.4 produces good agreement with more detailed time dependent calculations of $E_{\rm k}$ [19]. These ejecta masses are consistent with

---

[18] Which is the case if the SED of the magnetar is dominated by X-ray radiation, as in the Crab pulsar for instance (Weisskopf et al. 2000).
[19] We also investigated the sensitivity to this assumption by computing masses (as well as photospheric velocities and temperatures) also from $E_{\rm k} = 10^{51} + 0.4E^{\rm mag}$ where the 40% conversion to kinetic energy is a typical value (Woosley 2010). We found very small differences in the derived quantities.
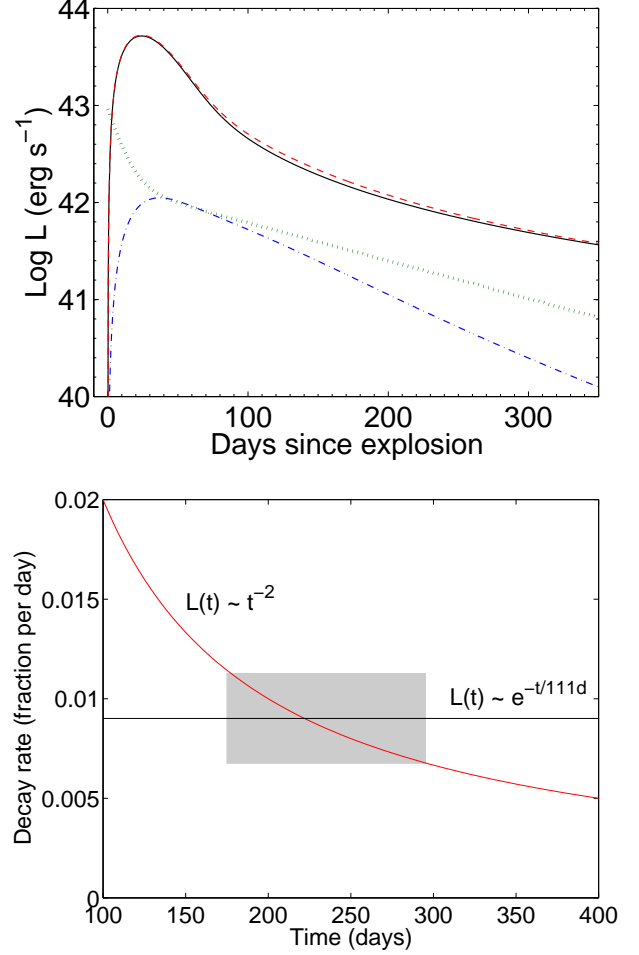

FIG. 14.— Top: Bolometric light curves for $B_{14} = 5$, $P_{\rm ms} = 5$, $M_{\rm ej} = 5\ M_\odot$ without ^{56}Ni contribution (black solid) and with M(^{56}Ni) $= 0.1\ M_\odot$ (red dashed). Also shown is the total energy emitted by M(^{56}Ni) $= 0.1\ M_\odot$ (green dotted) and the light curve produced by this amount of ^{56}Ni in a 5 $M_\odot$ ejecta with $E_{\rm k} = 10^{51}$ erg (blue dot-dashed). Bottom: Comparison between magnetar and ^{56}Co decay rate. The grey box is the region where the two slopes are similar to within 25%.

the ones derived for radioactivity-powered Type Ib/c ejecta (Ensman & Woosley 1988; Shigeyama et al. 1990; Valenti et al. 2011; Drout et al. 2011; Eldridge et al. 2013). Furthermore, Fig. 13 shows that the evolution of photospheric velocities and temperatures match the observed ones reasonably well. While the velocity and temperature evolution as estimated from our models are crude, this good agreement is an important test for the physical self-consistency of the model. From the lightcurve fits to ejecta mass and kinetic energy, we estimate the ejecta velocities ($V_{\rm core}$, see eq. D11) which we compare to the observed velocities of the emission lines (Ca H&K and Mg I] λ4571, see Tab. 3), finding them reasonably similar.

From the plot of bolometric light curves shown in Fig.6, it appears that there is a gap between the faintest SL-SNe Ic, and the brightest normal Type Ic. One possibility is that this is an observational bias. As SL-SNe Ic are intrinsically rare (Quimby et al. 2011a, 2013), we find them at moderate redshifts simply due to the large survey volume required to find them. If intermediate objects were

TABLE 4
Best-fit parameters for magnetar modelling of the bolometric light
curves and $\chi^2_{\rm red}$ value on the left. Derived parameters on the right.

Object	$\tau_{\rm m}$ (day)	B_{14}	$P_{\rm ms}$	t_0 (MJD)	$\chi^2_{\rm red}$	$E^{\rm mag}$ (10^{51} erg)	$M_{\rm ej}$ (M$_\odot$)	$V^{\rm final}_{\rm core}$ (km s^{-1})
SN 2011ke	35.0	6.4	1.7	55650.65	1.8	6.9	8.6	12400
SN 2011kf	15.4	4.7	2.0	55920.65	5.8	5.0	2.6	19600
SN 2012il	18.4	4.1	6.1	55918.56	3.9	0.5	2.3	10500
PTF10hgi	26.2	3.6	7.2	55322.78	0.5	0.4	3.9	7700
PTF11rks	21.0	6.8	7.5	55912.11	5.0	3.6	2.8	16500
SN 2010gx	32.4	7.4	2.0	55269.22	3.9	5.0	7.1	11900

also as rare, then we would require wider field searches to encompass more local volume as they may evade detection at the higher redshifts of known population of SL-SNe. An alternative explanation is that the mechanism powering the SL-SNe has a minimum energy. From the semi-analytic magnetar model of Kasen & Bildsten (2010) which we have used to match our light curves, we see that the peak magnetar luminosity is inversely proportional to the square of the magnetic field (eq. 4 Kasen & Bildsten 2010). Hence, the question arises, could the apparent lower luminosity limit to the SL-SNe Ic be caused by some physical upper limit to the magnetic field in a magnetar? For our faintest SL-SNe, and using a minimum plausible ejecta mass of 1 M$_\odot$, we determine an upper limit to the magnetar B-field of $B < 1.4 \times 10^{15}$ G from Eq. 4 of Kasen & Bildsten (2010). If we consider that Kasen & Bildsten (2010) assume an angle between the B field and the spin axis of the magnetar of 45°, then a factor of two higher than this value could be a plausible maximum. We hence adopt $B < 3 \times 10^{15}$ G.

The most conservative limit we can set is that the magnetic energy in the magnetar must be less than the gravitational binding energy of the neutron star (Chandrasekhar & Fermi 1953). This implies that

$$B < 10^{18} \left(\frac{\rm M_{NS}}{1.4~M_\odot} \right) \left(\frac{R_{NS}}{10~\rm km} \right)^{-2} \rm G \qquad (4)$$

which does not set a particularly stringent upper limit on the B-field. This limit is consistent with the B values retrieved from all the galactic magnetars studied so far which have $B \sim 10^{14} - 10^{15}$ G (Woods & Thompson 2006). However, magnetic fields are known to be a possible source of braking in stars (Meynet et al. 2011), while the magnetar models require an extreme magnetic field and fast rotational period. An explanation for both a small rotational period and a large magnetic field could be a large-scale helical dynamo, that is possible when the rotation period is comparable to the timescale of the convective motions (Duncan & Thompson 1992).

7. CONCLUSION

We have presented extensive photometric and spectroscopic coverage of five of the lowest redshift SL-SNe Ic. For one of them, SN 2011ke, we present a lightcurve from -30d to 200d, showing a well constrained rise time and a clear detection at 200d indicating a flattening of the luminosity. In four out of six SL-SNe, we show that there is significant luminosity in this late tail phase, and we illustrate that these measurements can aid our understanding of the power source and the possible progenitors of these ultra luminous transients.

The five SNe, namely PTF10hgi, SN 2011ke, PTF11rks, SN 2011kf and SN 2012il have absolute magnitudes $-21.73 \lesssim M_g(\rm mag) \lesssim -20.42$ similar to previous SL-SNe as well as a spectral evolution resembling SN 2010gx (Pastorello et al. 2010). There is some variation in the sample as two of the objects are fainter than the rest and spectroscopically evolve faster. PTF10hgi and PTF11rks have peak absolute magnitudes fainter than $M_g > -21$ mag. The spectra of PTF11rks evolves faster than the rest and at 10d post maximum it resembles a normal Type Ic at peak. In contrast, SN 2010gx and three other SNe presented here typically take 30 days to evolve to this phase. The latest spectrum we have of PTF10hgi shows well developed lines of Fe II at velocities which are more comparable with standard Type Ic SNe, significantly slower than the bulk of the SL-SNe Ic sample. Our *xshooter* spectrum of SN 2012il +52d is the only NIR spectrum of an SL-SNe Ic and we detect a broad He I λ10830 in emission implying that at least some SL-SNe Ic are not completely He-free. During the epochs of ± 10 d around peak the temperatures and velocities are nearly constant and do not show a clear decrease until after that period. We find that the decay timescale in the 100-200d period is similar to that expected from the radioactive decay of ^{56}Co, but it requires the γ-rays to be fully trapped. This is in contrast to the faster decline observed in most Type Ib/c SNe, where γ-ray leakage has a significant effect from 50 days onwards (Sollerman et al. 2000). Hence it is unlikely that this is due to large amounts (1-4 M$_\odot$) of ^{56}Ni produced in the explosion.

We applied a semi-analytical diffusion model with energy input from a spinning down magnetar to fit the lightcurves of our five objects and SN 2010gx, including the diffusion peak and the tail phase detections. All lightcurves, including the tail phases are reproduced with feasible physical values for a magnetar. powered SL-SN. We require $3.6 \lesssim B_{14} \lesssim 7.4$, $1.7 \lesssim P_{\rm ms} \lesssim 7.5$ consistent with B of known galactic magnetars ($B_{14} \sim 1 - 10$) and with physically plausible periods ($P_{\rm ms} > 1$). We derived energies of $0.4 \lesssim E^{\rm mag}(10^{51}$ erg$) \lesssim 6.9$ and ejected masses of $2.3 \lesssim M_{\rm ej}(\rm M_\odot) \lesssim 8.6$.

The well sampled data of the five SL-SNe Ic presented here combined with those of SN 2010gx point toward a SN explosion driven by a magnetar as a viable explanation for all the SL-SNe Ic. The lightcurves are reproduced and the model temperatures and velocities are in reasonable agreement with the observational data. However even if this is a reliable model, it still leaves other open questions such as

- Do H-rich SNe powered by magnetars exist[20] ? Possibly SN 2008es (Gezari et al. 2009) could be an example of such a luminous type II SN. In other words, why do we observe so many more H-free than H-rich SL-SNe?

- What is the role of metallicity in the progenitor stars evolution that will produce a H-free SL-SNe? It appears that they are all associated with faint dwarf galaxies and almost certainly low metallicity progenitors.

- Do realistic spectral calculations of magnetar driven SN reproduce the main observed features at late time?

- Where is the peak of the magnetar SED and how does the magnetar radiation deposit and thermalize in the nebular phase?

To address these, further observations are required combined with modelling. Theoretical modelling of high quality data in the nebular phase to determine the ejecta masses, composition and the mass of ^{56}Co contributing to the luminosity seems the most likely way to make progress. Optical spectroscopy at $\sim$300d post explosion appears to us to be the next step in probing the nature of these events. At $z \sim 0.1$, the typical AB magnitudes of these sources are $\sim 23 \pm 0.5$, requiring approximately 1 night of 8m telescope time to gather a spectrum with high enough signal-to-noise to measure the expected Ic-like emission lines with confidence.

REFERENCES

Abazajian, K. N., Adelman-McCarthy, J. K., Agüeros, M. A., et al. 2009, ApJS, 182, 543

Agnoletto, I., Benetti, S., Cappellaro, E., et al. 2009, ApJ, 691, 1348

Alard, C. 2000, A&AS, 144, 363

Ahn, C. P., Alexandroff, R., Allende Prieto, C., et al. 2012, ApJS, 203, 21

Arnett, W. D. 1982, ApJ, 253, 785

Barbary, K., Dawson, K. S., Tokita, K., et al. 2009, ApJ, 690, 1358

Barkov, M. V., & Komissarov, S. S. 2011, MNRAS, 415, 944

Baron, E., Hauschildt, P. H., Branch, D., Kirshner, R. P., & Filippenko, A. V. 1996, MNRAS, 279, 799

Berger, E., Chornock, R., Lunnan, R., et al. 2012, ApJ, 755, L29

Bersten, M. C., Benvenuto, O. G., Nomoto, K., et al. 2012, ApJ, 757, 31

Bersten, M. C., Benvenuto, O., & Hamuy, M. 2011, ApJ, 729, 61

Botticella, M. T., Trundle, C., Pastorello, A., et al. 2010, ApJ, 717, L52

Bouchet, P., Slezak, E., Le Bertre, T., Moneti, A., & Manfroid, J. 1989, A&AS, 80, 379

Blinnikov, S. I., & Sorokina, E. I. 2010, arXiv:1009.4353

Bucciantini, N., Quataert, E., Metzger, B. D., et al. 2009, MNRAS, 396, 2038

Cappellaro, E., Mazzali, P. A., Benetti, S., et al. 1997, A&A, 328, 203

Chandrasekhar, S., & Fermi, E. 1953, ApJ, 118, 116

Chatzopoulos, E., & Wheeler, J. C. 2012, ApJ, 760, 154

Chatzopoulos, E., Wheeler, J. C., & Vinko, J. 2012, ApJ, 746, 121

Chatzopoulos, E., Wheeler, J. C., & Vinko, J. 2009, ApJ, 704, 1251

Chen, T.-W., Smartt, S. J., Bresolin, F., et al. 2013, ApJ, 763, L28

Chevalier, R. A., & Irwin, C. M. 2011, ApJ, 729, L6

Chomiuk, L., Soderberg, A., Margutti, R., et al. 2012, The Astronomer's Telegram, 3931, 1

Chomiuk, L., Chornock, R., Soderberg, A. M., et al. 2011, ApJ, 743, 114

Dessart, L., Hillier, D. J., Waldman, R., Livne, E., & Blondin, S. 2012, MNRAS, 426, L76

Dexter, J., & Kasen, D. 2012, arXiv:1210.7240

Drake, A. J., Djorgovski, S. G., Mahabal, A. A., et al. 2012, The Astronomer's Telegram, 3873, 1

Drake, A. J., Djorgovski, S. G., Mahabal, A. A., et al. 2011, The Astronomer's Telegram, 3343, 1

Drake, A. J., Djorgovski, S. G., Mahabal, A., et al. 2009, ApJ, 696, 870

---

[20] Some studies in order to investigate the existence of H-rich SNe powered by magnetar have been done by Barkov & Komissarov (2011).

Drout, M. R., Soderberg, A. M., Gal-Yam, A., et al. 2011, ApJ, 741, 97

Duncan, R. C., & Thompson, C. 1992, ApJ, 392, L9

Eldridge, J. J., Fraser, M., Smartt, S. J., Maund, J. R., & Crockett, R. M. 2013, arXiv:1301.1975

Ensman, L. M., & Woosley, S. E. 1988, ApJ, 333, 754

Galama, T. J., Vreeswijk, P. M., van Paradijs, J., et al. 1998, Nature, 395, 670

Gal-Yam, A. 2012, Science, 337, 927

Gal-Yam, A., Mazzali, P., Ofek, E. O., et al. 2009, Nature, 462, 624

Gezari, S., Chornock, R., Rest, A., et al. 2012, Nature, 485, 217

Gezari, S., Rest, A., Huber, M. E., et al. 2010, ApJ, 720, L77

Gezari, S., Halpern, J. P., Grupe, D., et al. 2009, ApJ, 690, 1313

Ginzburg, S., & Balberg, S. 2012, ApJ, 757, 178

Hadjiyska, E., Rabinowitz, D., Baltay, C., et al. 2012, IAU Symposium, 285, 324

Hamuy, M. 2003, ApJ, 582, 905

Hamuy, M., Suntzeff, N. B., Gonzalez, R., & Martin, G. 1988, AJ, 95, 63

Herzig, K., El Eid, M. F., Fricke, K. J., & Langer, N. 1990, A&A, 233, 462

Hodapp, K. W., Siegmund, W. A., Kaiser, N., Chambers, K. C., Laux, U., Morgan, J., & Mannery, E. 2004, Proc. SPIE, 5489, 667

Hunter, D. J., Valenti, S., Kotak, R., et al. 2009, A&A, 508, 371

Kaiser, N., et al. 2010, Proc. SPIE, 7733, 12K.

Karp, A. H., Lasher, G., Chan, K. L., & Salpeter, E. E. 1977, ApJ, 214, 161

Kasen, D., & Bildsten, L. 2010, ApJ, 717, 245

Kotera, K., Phinney, E. S., & Olinto, A. V. 2013, arXiv:1304.5326

Law, N. M., Kulkarni, S. R., Dekany, R. G., et al. 2009, PASP, 121, 1395

Leloudas, G., Chatzopoulos, E., Dilday, B., et al. 2012, A&A, 541, A129

Magnier E.A., et al. 2013, ApJ, in press

Magnier, E. A., Liu, M., Monet, D. G., & Chambers, K. C. 2008, IAU Symposium, 248, 553

Magnier, E. 2007, The Future of Photometric, Spectrophotometric and Polarimetric Standardization, 364, 153

Mahabal, A. A., & Drake, A. J. 2010, The Astronomer's Telegram, 2508, 1

Margutti, R., Soderberg, A., Chomiuk, L., et al. 2012, The Astronomer's Telegram, 3925, 1

McKenzie, E. H., & Schaefer, B. E. 1999, PASP, 111, 964

Meynet, G., Eggenberger, P., & Maeder, A. 2011, A&A, 525, L11

Moriya, T. J., & Tominaga, N. 2012, ApJ, 747, 118

Neill, J. D., Sullivan, M., Gal-Yam, A., et al. 2011, ApJ, 727, 15

Ofek, E. O., Cameron, P. B., Kasliwal, M. M., et al. 2007, ApJ, 659, L13

Ostriker, J. P., & Gunn, J. E. 1971, ApJ, 164, L95

Pastorello, A., Smartt, S. J., Botticella, M. T., et al. 2010, ApJ, 724, L16

Patat, F., Cappellaro, E., Danziger, J., et al. 2001, ApJ, 555, 900

Poole, T. S., Breeveld, A. A., Page, M. J., et al. 2008, MNRAS, 383, 627

Prieto, J. L., Drake, A. J., Mahabal, A. A., et al. 2012, The Astronomer's Telegram, 3883, 1

Quimby, R. M., Yuan, F., Akerlof, C., & Wheeler, J. C. 2013, MNRAS, 431, 912

Quimby, R. M., Kulkarni, S. R., Kasliwal, M. M., et al. 2011a, Nature, 474, 487

Quimby, R. M., Gal-Yam, A., Arcavi, I., et al. 2011b, The Astronomer's Telegram, 3841, 1

Quimby, R. M., Sternberg, A., & Matheson, T. 2011c, The Astronomer's Telegram, 3344, 1

Quimby, R. M., Kulkarni, S., Ofek, E., et al. 2010, The Astronomer's Telegram, 2740, 1

Quimby, R. M., Aldering, G., Wheeler, J. C., et al. 2007, ApJ, 668, L99

Quimby, R. M., Castro, F., Gerardy, C. L., et al. 2005, Bulletin of the American Astronomical Society, 37, #171.02

Rau, A., Kulkarni, S. R., Law, N. M., et al. 2009, PASP, 121, 1334

Schlegel, D. J., Finkbeiner, D. P., & Davis, M. 1998, ApJ, 500, 525

Shigeyama, T., Nomoto, K., Tsujimoto, T., & Hashimoto, M.-A. 1990, ApJ, 361, L23

Shigeyama, T., & Nomoto, K. 1990, ApJ, 360, 242

Smartt, S. J., Wright, D., Valenti, S., et al. 2012, The Astronomer's Telegram, 3918, 1

Smartt, S. J., Valenti, S., Magill, L., et al. 2011, The Astronomer's Telegram, 3351, 1

Smith, N., Li, W., Foley, R. J., et al. 2007, ApJ, 666, 1116

Smith, N., & McCray, R. 2007, ApJ, 671, L17

Sollerman, J., Kozma, C., Fransson, C., et al. 2000, ApJ, 537, L127

Swartz, D. A., Wheeler, J. C., & Harkness, R. P. 1991, ApJ, 374, 266

Taubenberger, S., Pastorello, A., Mazzali, P. A., et al. 2006, MNRAS, 371, 1459

Thompson, T. A., Chang, P., & Quataert, E. 2004, ApJ, 611, 380

Tonry, J., & Onaka, P. 2009, Advanced Maui Optical and Space Surveillance Technologies Conference, Proceedings of the Advanced Maui Optical and Space Surveillance Technologies Conference, Ed.: S. Ryan, p.E40.

Tonry, J. L., Stubbs, C. W., Kilic, M., et al. 2012, ApJ, 745, 42

Tonry, J. L., Stubbs, C. W., Lykke, K. R., et al. 2012, ApJ, 750, 99

Umeda, H., & Nomoto, K. 2008, ApJ, 673, 1014

Usov, V. V. 1992, Nature, 357, 472

Valenti, S., Elias-Rosa, N., Taubenberger, S., et al. 2008, ApJ, 673, L155

Valenti, S., Smartt, S., Young, D., et al. 2010, The Astronomer's Telegram, 2773, 1

Valenti, S., Fraser, M., Benetti, S., et al. 2011, MNRAS, 416, 3138

Weisskopf, M. C., Hester, J. J., Tennant, A. F., et al. 2000, ApJ, 536, L81

Wheeler, J. C., Yi, I., Höflich, P., & Wang, L. 2000, ApJ, 537, 810

Woods, P. M., & Thompson, C. 2006, Compact stellar X-ray sources, 547

Woosley, S. E. 2010, ApJ, 719, L204

Woosley, S. E., Blinnikov, S., & Heger, A. 2007, Nature, 450, 390

Woosley, S. E., Hartmann, D., & Pinto, P. A. 1989, ApJ, 346, 395

York, D. G., Adelman, J., Anderson, J. E., Jr., et al. 2000, AJ, 120, 1579

Young, D. R., Smartt, S. J., Valenti, S., et al. 2010, A&A, 512, A70

Young, T. R. 2004, ApJ, 617, 1233

TABLE 5
Observed (non K-corrected) photometry of PTF10hgi plus associated errors in parentheses. Also reported are the host galaxy magnitudes, measured after the SN has faded.

Date	MJD	Phase[a]	u	g	r	i	z	Telescope
15/05/10	55331.61	-28.0			19.10 (-)			ATel 2740
18/05/10	55334.57	-25.3			18.90 (0.07)			PS1
26/05/10	55342.33	-18.2				18.49 (0.07)		PS1
26/05/10	55342.34	-18.2				18.48 (0.06)		PS1
15/06/10	55362.40	0.0		18.23 (0.05)				PS1
19/06/10	55366.45	3.7			18.04 (0.10)			PS1
20/06/10	55367.75	4.9			18.00 (-)			ATel 2740
21/06/10	55368.53	5.4				18.01 (0.05)		PS1
21/06/10	55368.55	5.4				18.02 (0.05)		PS1
13/07/10	55390.81	25.8	20.08 (0.12)					UVOT
17/07/10	55395.39	30.0		18.93 (0.05)	18.63 (0.08)	18.56 (0.05)	18.58 (0.14)	LT
18/07/10	55396.00	30.5	20.80 (0.15)					UVOT
20/07/10	55398.47	32.8		19.24 (0.08)	18.88 (0.09)	18.84 (0.08)	18.91 (0.10)	LT
23/07/10	55401.50	35.5		19.44 (0.08)	19.11 (0.09)	18.91 (0.08)	19.10 (0.10)	LT
27/07/10	55405.39	39.1		19.60 (0.05)	19.17 (0.06)	19.03 (0.03)	19.16 (0.10)	LT
31/07/10	55409.40	42.7		19.74 (0.02)	19.29 (0.03)	19.10 (0.04)	19.24 (0.10)	LT
14/08/10	55423.39	55.4		20.16 (0.03)	19.59 (0.03)	19.44 (0.04)	19.30 (0.10)	LT
17/08/10	55426.42	58.2		20.21 (0.04)	19.60 (0.05)	19.47 (0.05)	19.34 (0.11)	LT
19/08/10	55428.87	60.4		20.28 (0.17)	19.64 (0.07)	19.52 (0.05)	19.37 (0.09)	FTN
20/08/10	55429.43	60.9		20.33 (0.13)	19.66 (0.06)	19.53 (0.06)	19.39 (0.16)	LT
24/08/10	55433.38	64.5		20.40 (0.07)	19.70 (0.05)	19.60 (0.07)	19.40 (0.05)	LT
27/08/10	55436.40	67.3		20.48 (0.29)	19.77 (0.12)	19.62 (0.09)	19.44 (0.26)	LT
30/08/10	55439.82	70.4		20.49 (0.08)	19.83 (0.04)	19.64 (0.03)	19.48 (0.09)	FTN
01/09/10	55441.37	71.8		20.54 (0.01)	19.84 (0.04)	19.71 (0.05)	19.56 (0.05)	LT
05/09/10	55445.37	75.4		20.64 (0.04)	19.89 (0.04)	19.76 (0.06)	19.65 (0.07)	LT
07/09/10	55447.80	77.6		20.67 (0.03)	19.92 (0.04)	19.82 (0.03)	19.78 (0.07)	FTN
08/09/10	55448.38	78.2		20.70 (0.04)	19.97 (0.04)	19.87 (0.04)	19.83 (0.08)	LT
13/09/10	55453.77	83.1		20.85 (0.05)	20.06 (0.05)	19.97 (0.05)	20.04 (0.09)	FTN
20/09/10	55460.36	89.0		21.01 (0.08)[b]	20.21 (0.09)[b]		20.21 (0.13)[b]	LT
22/02/11	55615.21	229.8				23.82 (0.31)[b]		WHT
24/02/11	55616.23	231.2			23.92 (0.30)[b]			WHT
28/04/11	55679.56	288.3		>21.98				PS1
Host								
26/05/12	56073.00	646.0		23.64 (0.23)	22.01 (0.09)			WHT
28/05/12	56075.00	648.0				22.18 (0.15)	21.59 (0.15)	TNG

Note. — PS1 = 1.8 m Pan-STARRS1; UVOT = Swift + UVOT; LT = 2.0 m Liverpool Telescope + RATCam; FTN = 2.0 m Faulkes Telescope North + MEROPE; WHT = 4.2 m William Herschel Telescope + ACAM.
[a] phase with respect to the g-band maximum, corrected for time dilation
[b] magnitudes after image subtraction using 646-648d images

APPENDIX

TABLES

TABLE 6
Observed (non K-corrected) photometry of SN 2011ke and associated errors in parentheses, plus host (see Tab. 5).

Date	MJD	Phase[a]	u	B	g	V	r	i	z	Tel.
16/03/11	55637.00	-43.3				>20.10				CSS
30/03/11	55649.55	-32.3					>21.17			PS1
30/03/11	55650.50	-31.5			21.00 (-)					ATel
31/03/11	55651.58	-30.5						20.07 (0.06)		PS1
31/03/11	55651.60	-30.5						20.05 (0.06)		PS1
02/04/11	55653.57	-28.8					19.40 (0.05)			PS1
02/04/11	55653.58	-28.8					19.41 (0.05)			PS1
06/04/11	55657.99	-24.9				18.61 (0.08)				CSS
14/04/11	55665.98	-17.9				18.06 (0.07)				CSS
15/04/11	55666.80	-17.2			18.07 (0.08)		18.00 (0.06)	18.21 (0.08)		PS1
25/04/11	55677.00	-8.3				17.65 (0.07)				CSS
05/05/11	55686.50	0.0			17.70 (-)					ATel
12/05/11	55693.98	6.5				17.75 (0.06)				CSS
13/05/11	55694.99	7.4			18.08 (0.08)		17.91 (0.06)	18.15 (0.06)	18.20 (0.09)	LT
13/05/11	55695.54	7.9	18.34 (0.11)		18.08 (0.04)		17.92 (0.02)	18.10 (0.04)	18.13 (0.05)	FTN
15/05/11	55695.92	8.2		18.26 (0.09)		17.97 (0.08)				EKAR
14/05/11	55695.92	8.2			18.15 (0.08)		18.01 (0.10)	18.15 (0.09)	18.22 (0.12)	LT
14/05/11	55695.95	8.3			18.16 (0.08)		18.02 (0.04)	18.18 (0.04)	18.18 (0.09)	LT
14/05/11	55696.37	8.6	18.46 (0.20)							UVOT
15/05/11	55696.93	9.1			18.20 (0.14)		18.01 (0.06)	18.28 (0.08)	18.25 (0.20)	LT
16/05/11	55697.96	10.0	18.72 (0.17)		18.17 (0.05)		18.07 (0.06)	18.19 (0.03)	18.22 (0.04)	LT
17/05/11	55698.36	10.4	18.79 (0.24)		18.15 (0.07)		18.06 (0.06)	18.17 (0.04)	18.28 (0.05)	FTN
17/05/11	55698.95	10.9	18.95 (0.21)		18.29 (0.05)		18.05 (0.03)	18.26 (0.04)	18.16 (0.07)	LT
18/05/11	55700.04	11.8		18.62 (0.13)		18.11 (0.05)				EKAR
18/05/11	55700.05	11.8					18.10 (0.08)	18.25 (0.04)		LT
19/05/11	55700.90	12.6				18.14 (0.05)				EKAR
19/05/11	55700.94	12.6	19.08 (0.10)		18.41 (0.02)		18.18 (0.02)	18.26 (0.02)	18.35 (0.03)	LT
20/05/11	55702.03	13.6	19.23 (0.10)		18.46 (0.02)		18.19 (0.02)	18.26 (0.03)	18.43 (0.04)	LT
21/05/11	55702.97	14.4			18.54 (0.02)		18.22 (0.02)	18.31 (0.02)	18.37 (0.03)	LT
22/05/11	55703.93	15.2	19.31 (0.07)		18.60 (0.02)		18.30 (0.03)	18.34 (0.02)	18.42 (0.03)	LT
23/05/11	55704.92	16.1		18.94 (0.04)		18.35 (0.04)				EKAR
23/05/11	55704.93	16.1	19.33 (0.07)		18.65 (0.02)		18.33 (0.02)	18.42 (0.02)	18.45 (0.03)	LT
27/05/11	55708.95	19.6		19.20 (0.04)		18.55 (0.03)				EKAR
27/05/11	55709.40	20.0				18.56 (0.07)				CSS
28/05/11	55710.29	20.8	19.97 (0.03)		18.98 (0.04)		18.51 (0.02)	18.48 (0.03)	18.56 (0.06)	FTN
30/05/11	55710.37	20.9	20.08 (0.30)							UVOT
31/05/11	55712.94	23.1	20.08 (0.09)		19.13 (0.02)		18.60 (0.02)	18.61 (0.02)	18.62 (0.03)	LT
31/05/11	55712.97	23.2		19.45 (0.03)		18.73 (0.02)				EKAR
03/06/11	55715.93	25.7	20.25 (0.10)		19.30 (0.02)		18.77 (0.02)	18.71 (0.02)	18.70 (0.03)	LT
06/06/11	55719.37	28.8	20.79 (0.41)							UVOT
07/06/11	55719.98	29.3			20.03 (0.09)					EKAR
09/06/11	55721.93	31.0	21.69 (0.44)		19.79 (0.05)		19.09 (0.04)	19.06 (0.03)	19.05 (0.06)	LT
12/06/11	55724.50	33.2				19.25 (0.11)				CSS
17/06/11	55730.00	38.1		20.55 (0.08)		19.61 (0.04)				EKAR
24/06/11	55736.75	44.0	22.05 (0.12)	20.98 (0.06)		20.03 (0.04)	19.81 (0.04)	19.76 (0.05)		NTT
28/06/11	55740.90	47.6		21.24 (0.08)		20.33 (0.08)				EKAR
02/07/11	55745.33	51.5			21.40 (0.16)[b]		20.42 (0.07)[b]	20.07 (0.07)[b]	19.94 (0.08)[b]	FTN
09/07/11	55751.93	57.2			21.95 (0.16)[b]		20.99 (0.30)[b]	20.84 (0.17)[b]	20.64 (0.25)[b]	LT
13/07/11	55755.93	60.7		21.52 (0.24)		21.00 (0.27)				EKAR
23/07/11	55765.94	69.5			22.15 (0.06)[b]		21.26 (0.06)[b]	21.02 (0.07)[b]	20.86 (0.14)[b]	LT
24/07/11	55766.89	70.3			22.18 (0.08)[b]		21.28 (0.07)[b]	21.06 (0.07)[b]	20.88 (0.14)[b]	LT
25/07/11	55767.90	71.2			22.20 (0.06)[b]		21.32 (0.06)[b]	21.08 (0.07)[b]	20.91 (0.12)[b]	LT
03/08/11	55776.89	79.1			22.40 (0.11)[b]		21.48 (0.10)[b]	21.24 (0.08)[b]	21.07 (0.15)[b]	LT
21/12/11	55917.74	202.3			23.95 (0.30)[b]		23.14 (0.24)[b]	22.50 (0.20)[b]	22.30 (0.23)[b]	WHT
Host										
26/05/12	56073.50	338.6			21.18 (0.05)		20.72 (0.04)	20.47 (0.04)	20.90 (0.10)	WHT
12/06/04	53169.22		21.54 (0.24)		21.20 (0.08)		20.71 (0.08)	20.59 (0.11)	21.30 (0.67)	SDSS DR9

Note. — CSS = 0.7 m Catalina Schmidt Telescope; PS1 = 1.8 m Pan-STARRS1; LT = 2.0 m Liverpool Telescope + RATCam; FTN = 2.0 m Faulkes Telescope North + MEROPE; UVOT = Swift + UVOT; EKAR = 1.8 m Copernico Telescope + AFOSC; WHT = 4.2 m William Herschel Telescope + ACAM, NTT = 3.6m New Technology Telescope + EFOSC2, ATel = ATel 3344
[a] phase with respect to the g-band maximum, corrected for time dilation
[b] magnitudes after image subtraction using 339d images

TABLE 7
Observed (non *K*-corrected) photometry of PTF11rks and associated errors in parentheses, plus host (see Tab. 5).

Date	MJD	Phase[a]	u	g	r	i	z	Telescope
21/12/11	55916.70	-13.4			19.9 (-)			ATel 3841
27/12/11	55922.70	-8.4			19.1 (-)			ATel 3841
30/12/11	55925.24	-6.3	20.49 (0.12)					UVOT
01/01/12	55927.56	-4.3	20.30 (0.11)					UVOT
02/01/12	55929.42	-2.8		19.26 (0.09)	19.03 (0.20)			LT
03/01/12	55930.42	-1.9		19.19 (0.06)	18.94 (0.04)	19.14 (0.04)	19.25 (0.27)	LT
04/01/12	55931.34	-1.1		19.18 (0.04)	18.88 (0.03)	19.05 (0.08)	19.19 (0.24)	LT
05/01/12	55931.85	-0.7	20.46 (0.10)					UVOT
05/01/12	55932.72	0.0		19.13 (0.05)	18.87 (0.05)	19.01 (0.03)	19.14 (0.21)	FTN
08/01/12	55935.73	2.5		19.22 (0.04)	18.96 (0.02)	18.99 (0.04)	19.06 (0.06)	FTN
09/01/12	55936.40	3.1		19.23 (0.03)	18.97 (0.03)	19.00 (0.04)	19.06 (0.08)	LT
10/01/12	55936.71	3.4	20.55 (0.10)					UVOT
12/01/12	55939.32	5.6		19.30 (0.02)	19.03 (0.06)	18.97 (0.04)	19.03 (0.05)	LT
14/01/12	55941.32	7.2		19.37 (0.04)	19.04 (0.03)	18.98 (0.05)	19.07 (0.28)	LT
15/01/12	55941.51	7.4	20.93 (0.16)					UVOT
15/01/12	55942.35	8.1		19.38 (0.02)	19.04 (0.03)	18.98 (0.04)	19.09 (0.09)	LT
21/01/12	55948.75	13.5		19.65 (0.04)	19.19 (0.02)	19.08 (0.04)	19.10 (0.07)	FTN
24/01/12	55951.73	16.0		19.79 (0.04)	19.28 (0.03)	19.17 (0.05)	19.16 (0.06)	FTN
27/01/12	55954.44	18.3		19.93 (0.05)	19.41 (0.06)	19.22 (0.08)	19.17 (0.14)	LT
29/01/12	55956.84	20.3			19.46 (0.21)			FTN
04/02/12	55962.75	25.2		20.58 (0.14)	19.62 (0.04)	19.44 (0.03)	19.35 (0.03)	FTN
08/02/12	55966.74	28.6		20.90 (0.20)[b]	20.04 (0.08)[b]	19.84 (0.13)[b]	19.71 (0.16)[b]	FTN
03/03/12	55990.34	48.4			20.82 (0.15)[b]	20.55 (0.44)[b]		LT
26/06/12	56105.26	145.3		>22.9	>22.4	>22.1		WHT
Host								
22/09/12	56192.50	218.3		21.67 (0.07)	20.83 (0.05)			WHT
16/10/09	55121.47		21.51 (0.32)	21.59 (0.11)	20.88 (0.10)	20.71 (0.14)	20.03 (0.29)	SDSS DR9

Note. — Swift *u*-band data have been converted to SDSS magnitudes. UVOT = Swift +UVOT; LT = 2.0 m Liverpool Telescope +RATCam; FTN = 2.0 m Faulkes Telescope North +MEROPE; WHT = 4.2 m William Herschel Telescope +ACAM; GS = 8.1 m Gemini South +GMOS.
[a] phase with respect to the g-band maximum, corrected for time dilation
[b] magnitudes after image subtraction using 218d images or SDSS iz images

TABLE 8
Observed (non *K*-corrected) NIR photometry of PTF11rks plus associated errors in parentheses.

Date	MJD	Phase[a]	J	H	K	Telescope
07/02/12	55965.84	29.1			18.86 (0.10)	NOT
08/02/12	55966.88	30.0	19.31 (0.10)			NOT
09/02/12	55967.83	30.9	19.32 (0.10)			NOT
10/02/12	55968.84	31.8	19.42 (0.10)	19.41 (0.09)		NOT

Note. — NOT = 2.56 m Nordic Optical Telescope + NOTCam.
[a] phase with respect to the g-band maximum, corrected for time dilation

TABLE 9
Observed (non *K*-corrected) photometry of SN 2011kf and associated errors in parentheses,
plus host (see Tab. 5).

Date	MJD	Phase[a]	g	r	i	z	Telescope
30/12/11	55925.54	0.0	18.60 (0.08)				ATel 3873
25/01/12	55951.54	20.9	19.15 (0.08)				LT
21/02/12	55979.74	43.5	20.91 (0.08)	19.79 (0.06)	19.55 (0.05)	19.40 (0.10)	LT
22/02/12	55980.71	44.3	20.91 (0.11)	19.83 (0.05)	19.52 (0.07)	19.31 (0.10)	LT
23/02/12	55981.62	45.0	20.93 (0.05)				LT
24/02/12	55982.69	45.9	20.96 (0.11)	19.86 (0.06)	19.61 (0.06)	19.41 (0.06)	LT
08/03/12	55995.71	56.4		20.24 (0.08)	19.87 (0.10)	19.64 (0.21)	LT
10/03/12	55997.68	57.9	21.40 (0.19)	20.32 (0.11)	19.95 (0.09)	19.71 (0.19)	LT
12/03/12	55999.69	59.6	21.44 (0.19)	20.39 (0.10)	19.97 (0.08)	19.78 (0.12)	LT
13/03/13	56000.70	60.4	21.45 (0.10)	20.39 (0.05)	19.99 (0.11)	19.81 (0.19)	LT
18/03/12	56005.67	64.4	21.54 (0.09)	20.51 (0.06)	20.13 (0.09)	19.97 (0.10)	LT
23/03/12	56010.65	68.4	21.69 (0.16)	20.80 (0.10)	20.40 (0.15)	20.25 (0.19)	LT
27/03/12	56014.66	71.6	21.95 (0.11)	21.03 (0.12)	20.55 (0.18)	20.52 (0.20)	LT
24/05/12	56073.15	118.9	23.14 (0.21)[b]	22.07 (0.14)[b]	21.88 (0.13)[b]	21.81 (0.15)[b]	WHT
27/06/12	56106.04	145.4	>23.61	>22.7	>22.2	>22.0	WHT
Host							
27/06/12	56106.04	145.4				>22.0	WHT
20/07/12	56128.94	163.8	24.24 (0.34)	23.94 (0.30)	22.56 (0.33)		WHT
06/05/09	54987.25		>22.2	>22.2	>21.3	>20.5	SDSS DR9

Note. — LT = 2.0 m Liverpool Telescope +RATCam; WHT = 4.2 m William Herschel Telescope +ACAM.
[a] phase with respect to the g-band maximum, corrected for time dilation
[b] magnitudes after image subtraction using 163d images and SDSS griz images

TABLE 10
Observed (non *K*-corrected) photometry of SN 2012il and associated errors in parentheses, plus
host (see Tab. 5).

Date	MJD	Phase[a]	g	r	i	z	Telescope
31/12/11	55927.56	-11.8		18.75 (0.09)			CSS
05/01/12	55932.45	-7.6				18.99 (0.03)	PS1
05/01/12	55932.49	-7.6				18.96 (0.03)	PS1
14/01/12	55941.43	0.0		17.98 (0.06)			CSS
19/01/12	55946.44	4.3	18.34 (0.01)				PS1
21/01/12	55948.52	6.0		18.11 (0.07)			CSS
04/02/12	55961.54	17.1			18.94 (0.02)		PS1
05/02/12	55961.55	17.1			18.99 (0.02)		PS1
11/02/12	55969.56	23.9		18.96 (0.10)			CSS
20/02/12	55978.05	31.2	19.83 (0.03)	19.32 (0.09)	19.30 (0.07)	19.45 (0.12)	FTN
22/02/12	55980.56	33.3		19.35 (0.10)			CSS
23/02/12	55981.02	33.7	20.00 (0.05)	19.42 (0.04)			FTN
29/02/12	55987.48	39.2		19.74 (0.14)			CSS
14/03/12	56000.89	50.6	20.97 (0.07)	20.16 (0.07)	20.04 (0.08)	19.85 (0.09)	FTN
19/03/12	56005.86	54.8	21.11 (0.06)	20.25 (0.07)			FTN
20/03/12	56006.90	55.7	21.11 (0.07)	20.26 (0.05)	20.16 (0.05)	20.06 (0.14)	FTN
23/04/12	56009.89	58.3	21.19[b] (0.08)	20.35 (0.03)			FTN
24/03/12	56010.88	59.1	21.20[b] (0.09)	20.39 (0.08)	20.28 (0.12)	20.18 (0.09)	FTN
29/03/12	56015.86	63.3	21.29[b] (0.11)	20.47 (0.07)	20.40 (0.08)	20.30 (0.01)	FTN
26/05/12	56074.02	113.2		21.23 (0.20)[b]	21.00 (0.22)[b]	20.87 (0.20)[b]	WHT
Host							
10/02/13	56333.04	327.2	22.14 (0.17)	21.57 (0.06)	21.51 (0.08)	21.54 (0.35)	WHT
03/02/05	53405.24		22.13 (0.08)	21.46 (0.07)	21.64 (0.11)	21.50 (0.35)	SDSS DR9

Note. — CSS = 0.7 m Catalina Schmidt Telescope; PS1 = 1.8 m Pan-STARRS1; FTN = 2.0 m Faulkes
Telescope North + MEROPE; WHT = 4.2 m William Herschel Telescope + ACAM.
[a] phase with respect to the g-band maximum, corrected for time dilation
[b] magnitudes after image subtraction using 327d images

TABLE 11
Observed (non K-corrected) UVOT ultraviolet AB magnitudes of
SL-SNe Ic plus associated errors in parentheses.

Date	MJD	Phase[a]	uvw2	uvm2	uvw1
			PTF10hgi		
13/07/10	55390.31	25.8	21.93 (0.24)	22.05 (0.27)	20.97 (0.22)
18/07/10	55395.50	30.5	22.38 (0.43)	22.40 (0.44)	21.77 (0.29)
			SN 2011ke		
14/05/11	55695.87	8.6	20.67 (0.12)	20.42 (0.13)	18.86 (0.12)
30/05/11	55711.92	22.6	21.90 (0.21)	21.71 (0.17)	21.09 (0.21)
06/06/11	55718.87	28.7	22.01 (0.37)	21.63 (0.27)	
07/06/11	55719.73	29.6	22.27 (0.41)	22.14 (0.38)	21.53 (0.27)
08/06/11	55720.87	30.5	22.43 (0.48)	22.40 (0.49)	21.67 (0.43)
08/03/12	55994.99	270.3	>23.2	>23.1	>23.3
			PTF11rks		
30/12/11	55925.24	-6.2	20.92 (0.12)	21.12 (0.13)	20.42 (0.12)
01/01/12	55927.06	-4.6	21.22 (0.14)	21.52 (0.15)	20.45 (0.14)
05/01/12	55931.35	-0.8	21.47 (0.14)	21.59 (0.15)	21.17 (0.18)
10/01/12	55936.21	3.6	21.54 (0.15)	21.63 (0.20)	21.28 (0.20)
15/01/12	55941.01	7.8	22.00 (0.21)	21.68 (0.26)	21.42 (0.24)
			SN 2012il		
13/02/12	55971.71	25.3		22.14 (0.19)	21.33 (0.38)
14/02/12	55971.07	25.6	22.48 (0.26)		21.60 (0.26)

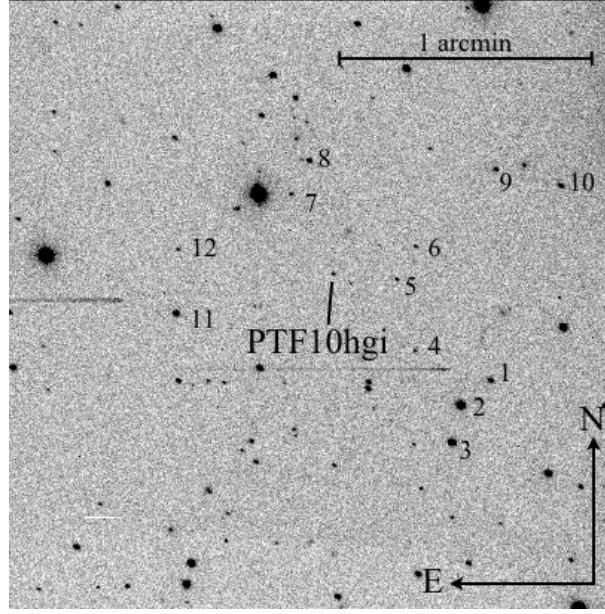[a] phases with respect to the g-band maxima, corrected for time dilation

Inserra et al.

Fig. 15.— *r*-band image of PTF10hgi obtained with LT + RATCam on September 5th, 2010. The sequence of stars used to calibrate the optical magnitudes is indicated by numbers.

TABLE 12
Magnitudes of the local sequence stars in the field of
PTF10hgi (cfr. Fig. 15).

ID	g	r	i	z
1	19.52 (0.05)	18.04 (0.03)	17.30 (0.03)	17.00 (0.04)
2	16.80 (0.01)	15.85 (0.02)	15.40 (0.02)	15.23 (0.02)
3	17.44 (0.02)	16.51 (0.02)	16.12 (0.02)	16.00 (0.02)
4	21.27 (0.08)	19.99 (0.05)	19.44 (0.05)	19.13 (0.05)
5	20.16 (0.05)	19.35 (0.05)	19.06 (0.04)	19.02 (0.05)
6	20.60 (0.06)	19.97 (0.05)	19.70 (0.05)	19.56 (0.07)
7	21.34 (0.08)	19.89 (0.05)	18.70 (0.04)	18.24 (0.05)
8	19.29 (0.04)	18.17 (0.04)	17.66 (0.03)	17.50 (0.05)
9	19.64 (0.05)	18.81 (0.04)	18.37 (0.03)	18.30 (0.05)
10	19.26 (0.04)	18.18 (0.04)	17.76 (0.03)	17.60 (0.05)
11	17.94 (0.03)	17.42 (0.03)	17.24 (0.03)	17.20 (0.04)
12	20.21 (0.06)	19.76 (0.05)	19.59 (0.05)	19.61 (0.06)

SEQUENCE STARS FOR PTF10hgi

Here we report the average magnitudes of the local sequence stars of PTF10hgi used to calibrate the photometric zero points for non-photometric nights. They are reported in Tab. 12 along with their r.m.s. (in brackets). Their positions are marked in Fig.15, along with the SN position.
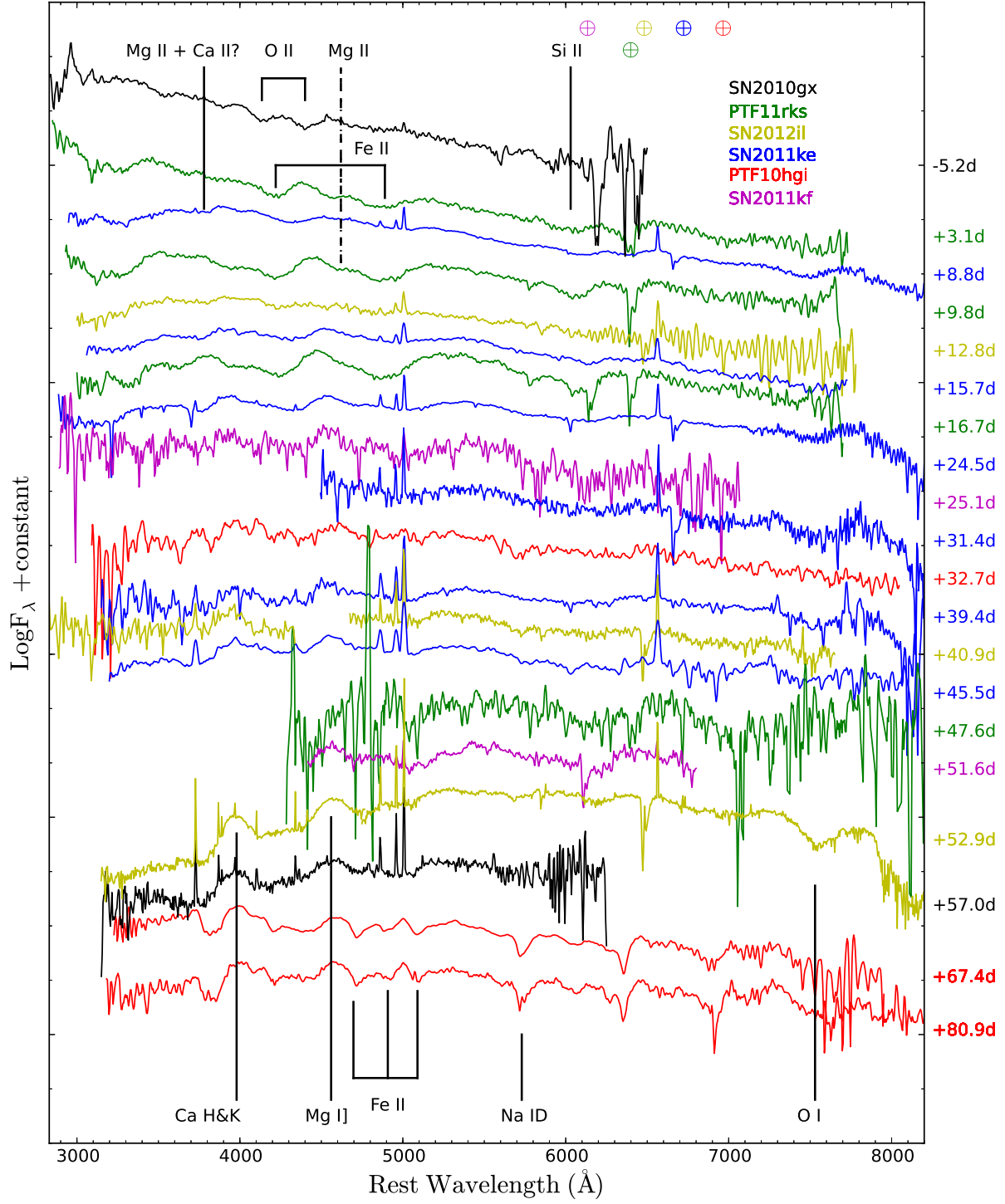
SPECTRAL EVOLUTION

FIG. 16.— Same figure as is Fig. 8 but with all the spectra convolved with a factor of five and subsequently binned to a 5 Å scale. Spectra of PTF11rks are in green, SN 2011ke in blue, SN 2012il in gold, PTF10hgi in red, SN 2011kf in magenta and SN 2010gx (Pastorello et al. 2010) in black. The phase of each spectrum relative to light curve peak in the rest frame is shown on the right. The spectra are corrected for extinction and reported in their rest frame. The most prominent features are labelled.

MAGNETAR-POWERED LIGHT-CURVES

Arnett (1982) derived the solution for the bolometric light-curve of a homologously expanding ejecta subject to a total (absorbed) power $P(t)$ as

$$L_{\rm SN}(t) = e^{-(t/\tau_{\rm m})^2} \int_0^{t/\tau_{\rm m}} P(t') 2 \, (t'/\tau_{\rm m}) \, e^{(t'/\tau_{\rm m})^2} \frac{dt'}{\tau_{\rm m}} \text{ erg s}^{-1}, \tag{D1}$$

where $\tau_{\rm m}$ is the diffusion time-scale parameter, which in the case of uniform density ($E_{\rm k} = \frac{3}{10} M_{\rm ej} V_{\rm ej}^2$) is

$$\tau_{\rm m} = \frac{1.05}{(\beta c)^{1/2}} \kappa^{1/2} M_{\rm ej}^{3/4} E_{\rm k}^{-1/4} \text{ s }. \tag{D2}$$

The parameter β has a typical value of 13.7 (Arnett 1982), which we use throughout. Apart from spherical symmetry and homology, the Arnett solution assumes a radiation pressure dominated gas, energy transport by diffusion, constant and grey opacity, and that the spatial distribution of energy input by the power source is proportional to the radiation energy density. The last assumption is for most cases the coarsest one, but the solutions are not critically dependent on deviations from it (Arnett 1982).

The power function $P(t)$ can generally be expressed as a sum of a set of source luminosities $L_i(t)$ multiplied by deposition functions $D_i(t)$:

$$P(t) = \sum L_{\rm i}(t) D_{\rm i}(t) \text{ erg s}^{-1}. \tag{D3}$$

For radioactivity from ^{56}Ni and its daughter nucleus ^{56}Co, the luminosity functions are

$$L_{56\rm Ni}(t) = 7.8 \cdot 10^{43} \left(\frac{M_{56\rm Ni}}{1 \, M_\odot} \right) e^{-t/\tau_{56\rm Ni}} \text{ erg s}^{-1}, \tag{D4}$$

$$L_{56\rm Co}(t) = 1.4 \cdot 10^{43} \left(\frac{M_{56\rm Ni}}{1 \, M_\odot} \right) \frac{e^{-t/\tau_{56\rm Co}} - e^{-t/\tau_{56\rm Ni}}}{1 - \frac{\tau_{56\rm Ni}}{\tau_{56\rm Co}}} \text{ erg s}^{-1}, \tag{D5}$$

where $M_{56\rm Ni}$ is the amount of ^{56}Ni formed in the explosion, and $\tau_{56\rm Ni}$ and $\tau_{56\rm Co}$ are the decay times of the isotopes (8.7 and 111 days, respectively).

For a magnetar with a 45-degree angle between the magnetic axis and spin axis, the dipole spin-down luminosity is (Ostriker & Gunn 1971; Kasen & Bildsten 2010)

$$L_{\rm magnetar}(t) = 4.9 \cdot 10^{46} B_{14}^2 P_{\rm ms}^{-4} \frac{1}{\left(1 + t/\tau_p\right)^2} \text{ erg s}^{-1}, \tag{D6}$$

where B_{14} is the magnetic field strength in 10^{14} G, $P_{\rm ms}$ is the initial spin period in ms, and the spin-down time-scale $\tau_{\rm p}$ is

$$\tau_p = 4.7 \, B_{14}^{-2} P_{\rm ms}^2 \text{ days }. \tag{D7}$$

With only magnetar powering, the light-curve parameters are thus τ_m, B_{14} and $P_{\rm ms}$. For a given fit to $\tau_{\rm m}$, the ejecta mass is (from Eq. D2)

$$M_{ej} = 1 \, M_\odot \cdot \left(\frac{\tau_{\rm m}}{10 \text{ d}} \right)^{4/3} \left(\frac{\kappa}{0.1 \text{ cm}^2 \text{g}^{-1}} \right)^{-2/3} \left(\frac{E_{\rm k}}{10^{51} \text{ erg}} \right)^{1/3} \tag{D8}$$

The weak scaling with κ and E_k means that ejecta masses can be meaningfully estimated despite significant uncertainties in κ and $E_{\rm k}$.

When the energy input $\int P(t)dt$ approaches or exceeds the explosion energy, accelerations will not be negligible and the homologous approximation becomes poor. A solar mass of ^{56}Ni emits a total energy of $\int P(t)dt = 1.9 \cdot 10^{50}$ erg (including the ^{56}Co decay), so for an explosion energy of $\sim 10^{51}$ erg, accelerations will not be important unless M(^{56}Ni)$\gtrsim 5 \, M_\odot$. A magnetar, on the other hand, has a rotation energy of $2 \cdot 10^{52} P_{\rm ms}^{-2}$ erg, so for fast braking with efficient trapping, the ejecta can be accelerated to far beyond its explosive velocities. This is a major limitation of using the homologous expansion approximation, and the consequences for the light curve can only be investigated with numerical radiation hydrodynamics (see Bucciantini et al. 2009, and reference therein for some examples).

The opacity

The opacity due to electron scattering is

$$\kappa_{\rm es} = 0.2 \left(\frac{\bar{Z}/\bar{A}}{0.5} \right) \left(\frac{x_{\rm e}}{\bar{Z}} \right) \text{ cm}^2 \text{ g}^{-1}, \tag{D9}$$

where $\bar{Z}$ is the mean atomic charge, $\bar{A}$ is the mean atomic mass, and $x_{\rm e} = n_{\rm e}/n_{\rm nuclei}$ is the ionization fraction. For any chemical mixture excluding hydrogen, $\bar{Z}/\bar{A} \approx 0.5$, which we can assume since there is no trace of hydrogen lines in

the spectra of these objects. The radiation temperature in a radiation-pressure dominated uniform sphere of internal energy $E(t)$ is

$$T(t) = \left(\frac{E(t)}{a \frac{4\pi}{3} V_{\mathrm{ej}}^3 t^3} \right)^{1/4} \sim 10^5 K \left(\frac{E(t)}{10^{51} \mathrm{\ erg}} \right)^{-1/8} \left(\frac{M}{1\ M_\odot} \right)^{3/8} \left(\frac{t}{10\mathrm{\ d}} \right)^{-3/4} \tag{D10}$$

In LTE, and at relevant densities here, the ionization fraction of a pure oxygen plasma at $T = 10^5$ K is $x_{\mathrm{e}} \sim 6$, for carbon it is $x_{\mathrm{e}} \sim 4$, and for Fe is $x_{\mathrm{e}} \sim 10$. It should thus be a reasonable approximation to use $x_{\mathrm{e}}/\bar{Z} = 0.5$. With this choice $\kappa_{\mathrm{es}} = 0.1$ cm^2 g^{-1}, comparable to the value $\kappa = 0.08$ that Arnett (1982) uses.

In rapidly expanding media, line opacity can become comparable to or exceed electron scattering opacity (Karp et al. 1977), which complicates analytical light curve modelling. A common simplistic approach to take line opacity into account is to put a minimum value on the opacity. In previous works, values ranging between 0.01 and 0.24 cm^2 g^{-1} have been used (e.g., Herzig et al. 1990; Swartz et al. 1991; Young 2004; Bersten et al. 2011, 2012). The implication of line opacity is that κ is likely to stay in the 0.01 - 0.2 cm^2 g^{-1}range throughout the evolution, and $\kappa = 0.1$ cm^2 g^{-1} is probably not off by more than a factor of a few at any given time.

Deposition of magnetar radiation

The spectral and directional distribution of the magnetar radiation is highly uncertain. At early times, most radiation will undoubtedly be absorbed, but at later times, this is not certain (Kotera et al. 2013). X-rays are efficiently absorbed for a long time by photoionization from inner shell electrons, but gamma rays see a smaller opacity and start escaping after a few weeks for typical ejecta parameters.

Here, we assume full trapping of the magnetar radiation. Most of the energy input occurs over a few weeks after explosion, and it is a reasonable assumption that most of the energy emerges as X-rays, as in the Crab pulsar for instance (Weisskopf et al. 2000).

Photospheric velocities and temperatures

To estimate the photospheric velocities and temperatures for a given solution for ejecta mass, we approximate the ejecta density structure with a core + envelope morphology. The velocity of the homogenous core (which contains almost all the mass to force consistency with the diffusion calculation) is determined from

$$\frac{3}{10} M_{\mathrm{ej}} V_{\mathrm{core}}^2 = E_{\mathrm{k}} \tag{D11}$$

and its density is given by

$$\rho_{\mathrm{core}}(t) = \frac{M_{\mathrm{ej}}}{\frac{4\pi}{3} V_{\mathrm{core}}^3 t^3} \ . \tag{D12}$$

Outside we attach an envelope with density profile

$$\rho(t, V) = \rho_{\mathrm{core}}(t) \left(\frac{V}{V_{\mathrm{core}}} \right)^{-\alpha} \tag{D13}$$

The optical depth of the envelope is

$$\tau_{\mathrm{env}} = \int_{R_{\mathrm{core}}}^{\infty} \rho_{\mathrm{core}} \left(\frac{r}{R_{\mathrm{core}}} \right)^{-\alpha} \kappa dr \tag{D14}$$

$$= \frac{\rho_{\mathrm{core}} R_{\mathrm{core}} \kappa}{\alpha - 1} \tag{D15}$$

$$= \frac{\tau_{\mathrm{core}}}{\alpha - 1} \tag{D16}$$

where

$$\tau_{\mathrm{core}}(t) = \kappa \rho_{\mathrm{core}}(t) V_{\mathrm{core}} t \ . \tag{D17}$$

One should in general distinguish between the photosphere and the thermalization layer, where the temperature of the continuum is determined. The position of these depend on the total opacity κ, and the absorption opacity κ_{a}, respectively. However, due to our simple treatment such detail is unwarranted, and we approximate them to be the same, R_*. As long as the atmosphere is optically thick ($\tau_{\mathrm{env}} > 1$), $R_*(t)$ is found from solving

$$\int_{R_*(t)}^{\infty} \kappa \rho(r, t) dr = 1 \ , \tag{D18}$$
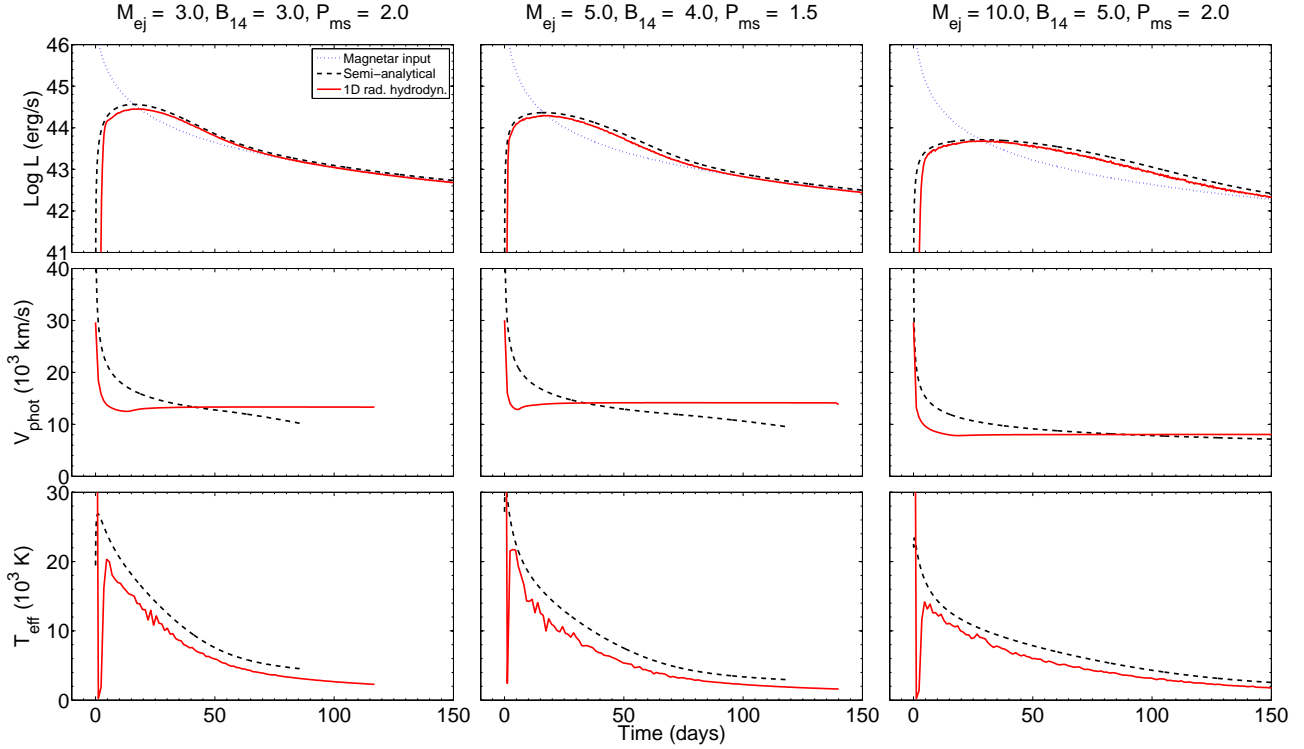
which gives

FIG. 17.— Comparison of light curves, photospheric velocities, and photospheric temperatures from our semi-analytical model (black, dashed) and the 1D radiation hydrodynamical simulations of Kasen & Bildsten (2010) (red, solid). Also shown is the input magnetar energy (blue, dotted line).

$$R_*(t) = R_{\mathrm{core}}(t) \left(\frac{\alpha - 1}{\tau_{\mathrm{core}}(t)} \right)^{\frac{1}{1-\alpha}} . \tag{D19}$$

If the photosphere has receded into the core, the expression is instead

$$R_*(t) = R_{\mathrm{core}}(t) - \frac{1 - \frac{\tau_{\mathrm{core}}}{\alpha - 1}}{\kappa \rho_{\mathrm{core}}} \tag{D20}$$

Typical density profiles in Ib/c models show $\alpha \sim 10$ (e.g. Fig. 1 in Kasen & Bildsten 2010), which is the value we use here.

From the photospheric radius $R_*(t)$ we retrieved the velocity at the photosphere (V_{phot})

$$V_{\mathrm{phot}}(t) = V_{\mathrm{core}} \frac{R_*(t)}{R_{\mathrm{core}}(t)}. \tag{D21}$$

The effective temperature is found from application of the black-body formula, using the model luminosities at corresponding times.

Additional tests

To test the applicability of our approach, we perform three tests. The first one is to compare light-curves, photospheric velocities and temperatures to the radiation hydrodynamical simulations of Kasen & Bildsten (2010). Fig. 17 shows three representative examples. For these comparisons, we use eq. 3 to relate magnetar energy to ejecta kinetic energy, which shows itself a good approximation. Tab. 13 shows the derived parameters of M_{ej}, B_{14}, P_{ms} and Δt for a series of simulations in Kasen & Bildsten (2010). The magnetar properties (B_{14} and P_{ms}) are reliably recovered to within 10-20% of their input values, whereas the ejecta mass can vary, tending to be too low in the fits. It is, however, always within a factor 2 of the correct value.

The second test is to derive parameters for the Type IIb SN 2011dh, using the approach described above (fixing $E_{\mathrm{k}} = 10^{51}$ erg, $\kappa = 0.1$, $\alpha = 10$). The best-fit is shown in Fig. 18. The recovered values $M_{\mathrm{ej}} = 2.2$ $M_\odot$ and $M_{56\mathrm{Ni}} = 0.08$ $M_\odot$ agree well with the results from Bersten et al. (2011), who used radiation hydrodynamical simulations.

While for the third one we tried to test our code on Type Ic SNe 1998bw (Galama et al. 1998; McKenzie & Schaefer 1999; Sollerman et al. 2000; Patat et al. 2001) and 2007gr (Valenti et al. 2008; Hunter et al. 2009) to explore its limits.

TABLE 13
BEST-FITTING VALUES OF SYSTEM PARAMETERS
(AFTER THE SLASH) COMPARED TO THE ACTUAL
SIMULATION VALUES OF KASEN & BILDSTEN (2010)
(BEFORE THE SLASH). DERIVED PARAMETERS ON
THE RIGH.

$M_{\rm ej}$	B_{14}	$P_{\rm ms}$	Shift (days)	$E^{\rm mag}$
3.0/3.0	2.0/2.2	2.0/2.3	$-1.57/0$	3.9
3.0/3.1	3.0/3.2	2.0/2.3	0.17/0	4.0
3.0/2.8	5.0/5.4	2.0/2.4	$-0.038/0$	3.6
5.0/3.1	3.0/3.2	2.0/2.3	0.18/0	3.9
5.0/3.0	4.0/4.3	2.0/2.4	7e$-$4/0	3.7
5.0/3.0	5.0/5.4	2.0/2.4	0.18/0	3.7
7.0/4.1	2.0/2.1	1.5/1.8	$-0.039/0$	6.6
7.0/3.8	3.0/3.2	1.5/1.9	-4.9e$-4/0$	6.1
10/12.8	2.0/2.7	2.0/1.6	$-5.0/0$	8.0
10/9.2	3.0/3.5	2.0/2.2	$-3.6/0$	4.3
10/7.4	5.0/5.1	2.0/2.9	1.8e$-4/0$	2.4

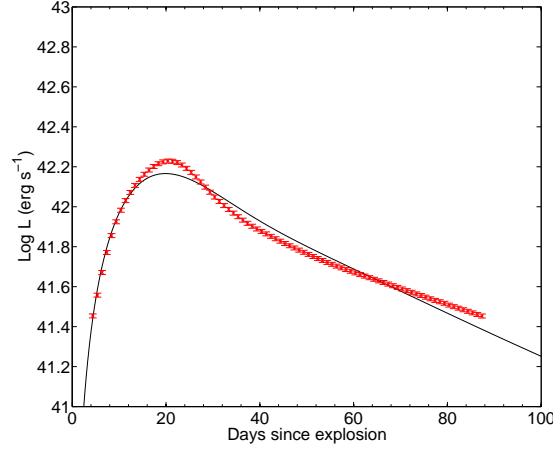FIG. 18.— Fit to the bolometric light curve of SN 2011dh (Ergon+, in prep). The fit values are $M_{\rm ej} = 2.2\ M_{\odot}$ and $M_{56\rm Ni} = 0.08\ M_{\odot}$, for $E_{\rm k} = 10^{51}$ erg and $\kappa = 0.1$ cm^2 g^{-1}.

TABLE 14
BEST-FIT PARAMETERS FOR ^{56}NI MODELLING OF THE BOLOMETRIC
LIGHT CURVES AND $\chi^2_{\rm red}$.

Object	Shift (day)	M(^{56}Ni) ($M_{\odot}$)	$M_{\rm ej}$ ($M_{\odot}$)	E (10^{51} erg)	t_0 (MJD)	$\chi^2_{\rm red}$
SN 2011ke	36.0	3.0	6.1	8.1	55650.65	35
SN 2011kf	38.0	5.0	11	15.0	55920.65	58
SN 2012il	26.0	2.9	5.9	6.2	55918.56	193
PTF10hgi	37.0	2.6	5.9	6.2	55322.78	1.2
PTF11rks	31.0	3.0	6.1	8.1	55912.11	53
SN 2010gx	50.0	6.0	13.0	15.0	55269.22	860

We fitted the first 200d with the magnetar model (fixing $E_{\rm k} = 10^{51}$ erg, $\kappa = 0.1$, $\alpha = 10$), recovering $M_{\rm ej} = 1.8\ M_{\odot}$ and $B_{14} = 9.8$ G and $P_{\rm ms} = 18.9$ ms for SN 1998bw and $M_{\rm ej} = 1.3\ M_{\odot}$ and $B_{14} = 22.9$ G and $P_{\rm ms} = 47.6$ ms for SN 2007gr. Instead, trying to fit the entire dataset, we recover $M_{\rm ej} = 19.9\ M_{\odot}$ and $B_{14} = 16.6$ G and $P_{\rm ms} = 0.5$ ms for SN 1998bw and $M_{\rm ej} = 2.5\ M_{\odot}$ and $B_{14} = 26.0$ G and $P_{\rm ms} = 42.6$ ms for SN 2007gr. The best fit to those data are shown in Fig. 19 along with the fit of the radioactive decay. The applicability of the Arnett model to derive parameters for radioactivity-driven SNe has also been demonstrated by Valenti et al. (2011). The results imply that at those energies the magnetar contribution is more important after 150-200 d, highlighting the importance of obtaining late time data.

^{56}Ni fits parameters

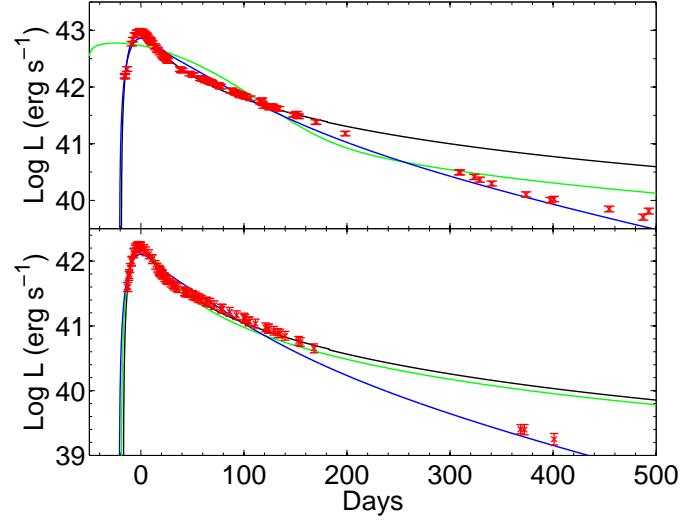For the ^{56}Ni models we computed γ-ray trapping as in Arnett (1982).

FIG. 19.— Fit to the bolometric light curve of SNe 1998bw (top) and 2007gr (bottom). Magnetar fit of the first 200d is shown (black) along with the fit of the entire set (green) and the fit of radioactive decay (blue). Both models can fit the first 50-100d but are clearly differentiated at late times